Supporting Information

1. CO$_2$, CH$_4$ AND TOTAL CONVERSION

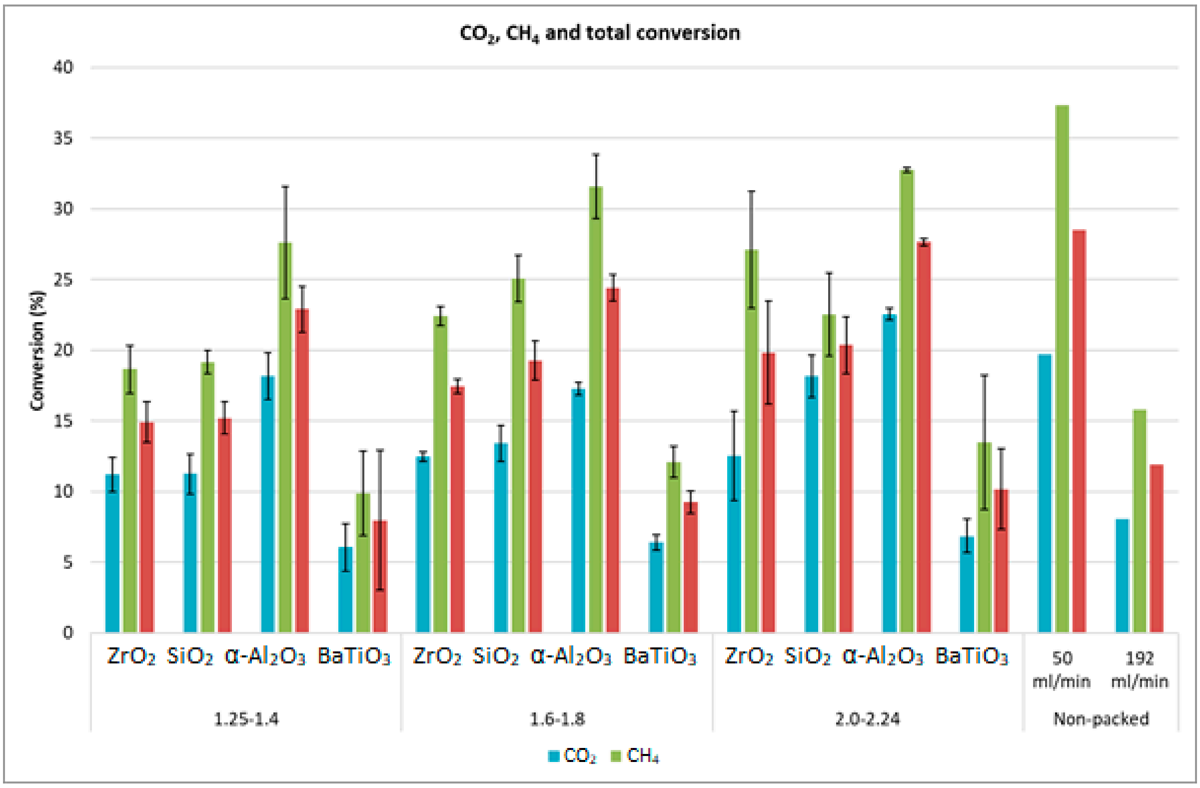

Figure S.1: CO2, CH4 and total conversion for different sphere sizes and materials, compared to the results for the non-packed reactor, at the same flow rate (50 ml/min) and at the same residence time (5,52 s; flow rate of 192 ml/min).

2. ELECTRICAL AND MATERIAL CHARACTERISATION

Table S.1: Physical and chemical characteristics of the packing materials

	BaTiO$_3$	**ZrO$_2$**	**SiO$_2$**	**α-Al$_2$O$_3$**	**γ-Al$_2$O$_3$**
Molar mass (g/mol)	233.20	123.22	60.08	101.96	101.96
Density (g/cm^3)	6.02	5.70	2.20	3.89	3.65
Thermal conductivity (W/m.K)[a]	2.85	1.70	1.38	28.0 - 35.0	28.0 - 35.0
Thermal expansion coefficient (10^{-6}/°C)[a]	11.4	12.2	0.550	5.8-8	5.8-8
Specific heat capacity (J/(g.K))[b]	0.406	0.456	0.99	0.798	0.850
***Band gap* (eV)[c]**	3.2	4.2	8.9	7.0	8.7
Dielectric strength (10^6 V/m)[a]	>30.0	5	32.5	8	8
Dielectric constant[a]	4000	23.0	3.9	9.00	9.00
Molar heat (J/(mol.K))[a]	94.68	56.23	59.64	81.38	108.7
BET specific surface (m^2/g)[d]	0.8	0	0.5	0.08	336

Total open pore volume (mm^3/g)[e]	158.0	≈0	≈0	8.47	500
Pore size (μm)[e]	0.87	≈0	≈0	0.080	0.54
Surface roughness (nm)[f]	590[1]±15	84±1	82±3	150±4	/
Plasma power (Watt)[g]	65±2	62±3	64±1	58±2	60±0
Burning voltage (kV)[g]	2.2±0.1	2.5±0.2	2.8±0.1	2.9±0.2	2.9±0.1

a: Taken from [1–10]

b: Calculated from the molar heath and the molar mass

c: Obtained from UV-vis DR spectra, for milled spheres (Figure S.2**, Figure S.**3 **and Figure S.**4**)**

d: Obtained from nitrogen sorption (Figure S.5 **- Figure S.**9**)**

e: Obtained from Hg-porosimetry, for 1.6-1.8 mm spheres (Figure S.10**- Figure S.**14**)**

f: Obtained from profilometry, for 2.0-2.24 mm spheres in collaboration with ULB [11]

g: Obtained by analysing the Lissajous-data (averaged out on the different sphere sizes)

Table S.2: Electrical characterisation for all experiments

Conditions		Plasma Power (W)	U_{bur} (kV)	U_{pp} (kV)	Average charge per filament (nF)	Number of discharges	I_{RMS} (mA)
Non-packed reactor	50 ml/min	62.86	3.861	15.09	16834	20.05	28.11
	192 ml/min	62.33	4.168	15.08	14243	24.93	27.68
SiO_2	1.25 - 1.4 mm	61.87	2.690	13.19	21534	85.97	36.03
	1.6 - 1.8 mm	62.38	2.797	12.56	5020	92.10	36.26
	2.0 - 2.24 mm	65.16	2.945	12.46	4331	114.67	36.14
ZrO_2	1.25 - 1.4 mm	61.87	2.690	13.19	5397	85.97	36.03
	1.6 - 1.8 mm	63.53	2.344	12.64	4618	128.65	45.18
	2.0 - 2.24 mm	62.95	2.498	12.04	3610	155.46	43.05
α-Al_2O_3	1.25 - 1.4 mm	55.22	2.787	17.16	3214	131.31	35.28
	1.6 - 1.8 mm	59.87	2.772	16.81	4182	112.25	37.15
	2.0 - 2.24 mm	59.18	3.076	16.75	2918	131.27	34.16
γ-Al_2O_3	-						
	-						
	2.0 - 2.24 mm	59.99	2.861	14.353	3469	146.58	36.98
$BaTiO_3$	1.25 - 1.4 mm	63.96	2.077	11.541	5365	132.67	50.77
	1.6 - 1.8 mm	65.28	2.187	11.576	5300	135.91	49.95
	2.0 - 2.24 mm	66.94	2.240	11.266	5240	131.00	49.98

Table S.1 summarises a non-limitative list of possible influencing material characteristics, based on measured data (e.g. UV-DR, N_2-sorption and Hg-porosimetry) and literature values. In the rest of section 1, the graphs of the measured data can be found.

The material characteristics of the different packing materials will influence the results obtained in this work, i.e. both conversion and product fractions/selectivities. Even though we cannot yet identify which material properties are responsible for the differences in the plasma chemistry, we have measured those properties, from which we expect a possible influence on the results. Therefore, all packing materials are studied with UV-DR (photon absorption, band gap), profilometry (surface roughness), nitrogen sorption (micro- and mesoporosity, surface area), Hg-porosimetry (meso- and macroporosity), SEM-EDX (chemical composition) and TGA (e.g. thermal stability and presence of surface adsorbed species). The specifics of the equipment are listed in Table S.3.

Table S.3: Specifics of the equipment for all characterization techniques

UV-DR	Thermo-electron evolution 500 UV-VIS spectrometer, using a Thermo-electron RSA UC40 Diffuse Reflectance cell. The samples were crushed, and the powder was diluted (2 wt% sample in 98 wt% KBr).
Profilometry	Brücker Dektak XT stylus profiler (measured at ULB)
N_2-sorption	Quantachrome Autosorb Degasser and Quantachrome Quadrasorb SI. Degassing took place during 16 hours, at 150 ºC, and 2×10^{-5} bar
Hg-porosimetry	Mercure Intrusion Porosimetry (Pascal 140, Thermo Scientific, USA) (measured at VITO)
TGA	Mettler Toledo TGA/SDTA851, O_2-flow, 30-800 ºC, 10 K/min
SEM EDX	Quanta 250 FEG ESEM (high-vacuum)

2.1 UV-DR

By comparing the UV-DR spectrum (Figure S.2) before and after plasma exposure, we can see that there is no significant change in the intersection of the tangent of the Tauc plot with the x-axis. The band-gap of the material thus remains unaltered after plasma exposure. The band gap of the tested SiO_2 spheres was calculated as 3.4 eV, which is lower than the band gap for amorphous SiO_2 (9.2 eV). The SiO_2 spheres are assumed to be glass, containing mostly Na, Ca, Mg. This is confirmed by the analysis with SEM-EDX (Table S.4).

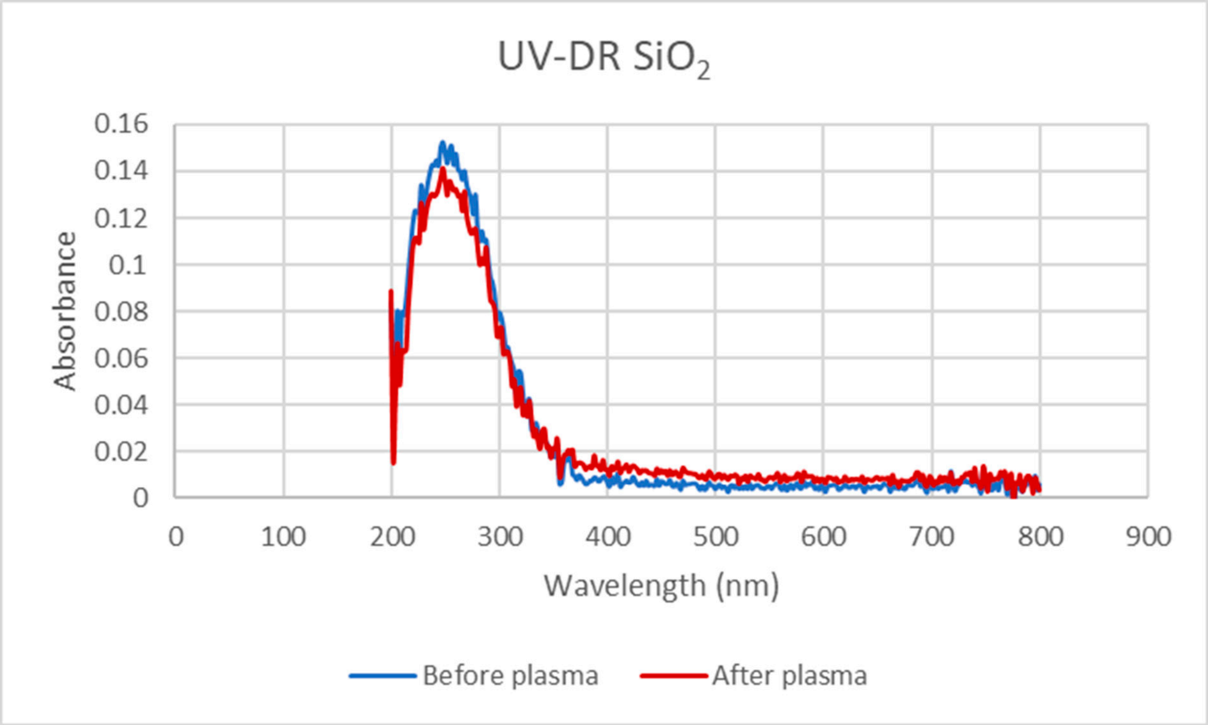

Figure S.2: UV-DR spectra of SiO_2 before (blue graph) and after (red graph) plasma exposure (milled spheres)

The UV-DR spectrum of ZrO_2 (Figure S.3) shows a bandgap of 4.3 eV, which remains unaltered after plasma exposure.

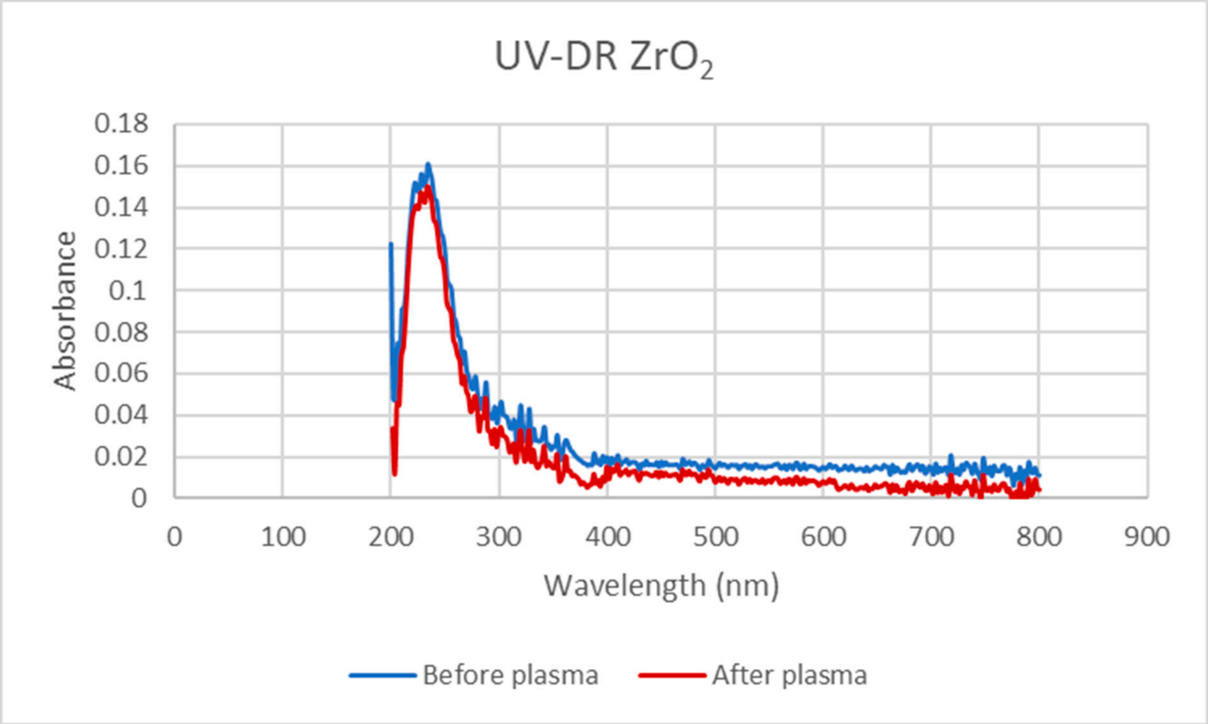

Figure S.3: UV-DR spectra for ZrO_2 before (blue graph) and after (red graph) plasma exposure (milled spheres)

α-Al_2O_3 is not active in UV-DR.

The UV-DR spectra (Figure S.4) for the $BaTiO_3$ spheres before and after plasma lead to the same band gap: 2,98 eV; the band-gap of the material thus remains unaltered after plasma exposure. The literature gives a value of 3.2 eV for tetragonal $BaTiO_3$[12]. At the moment we cannot explain this discrepancy in values, but it might be dependent on the crystal phase and/or structural composition[13,14].

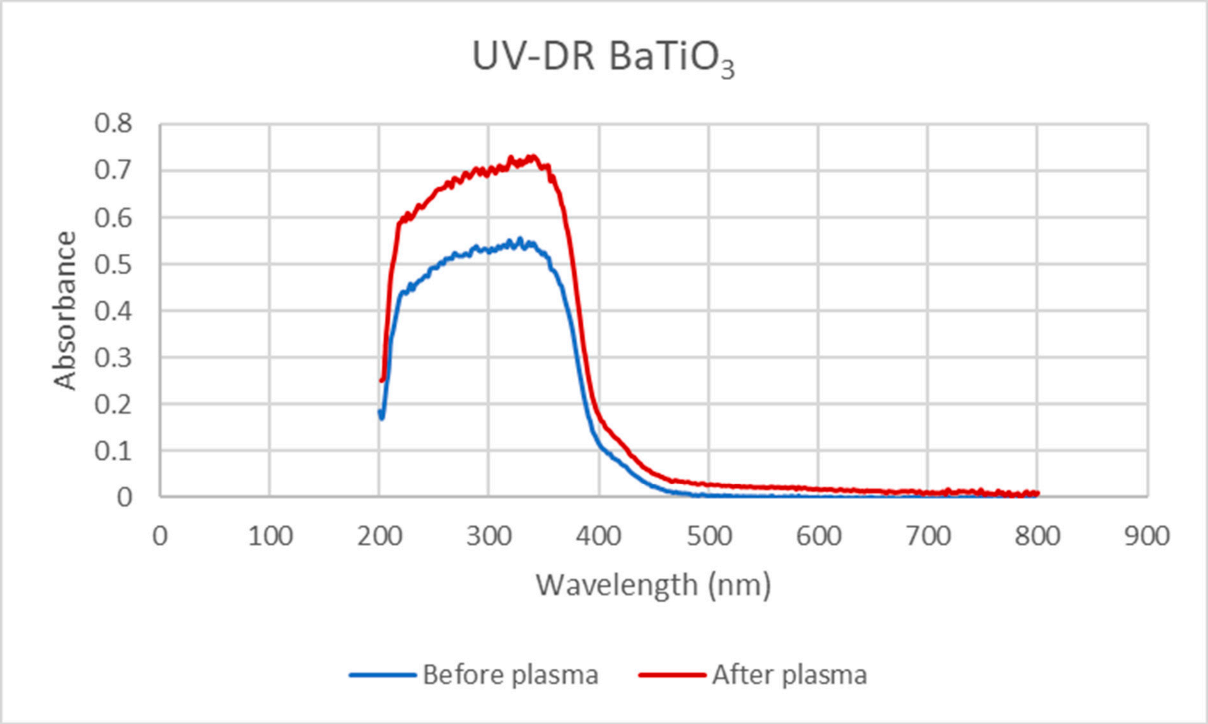

Figure S.4: UV-DR spectra for $BaTiO_3$ before (blue graph) and after (red graph) plasma exposure (milled spheres)

2.2 N_2-sorption

The nitrogen-sorption isotherms, used to calculate the apparent surface area of the SiO_2, ZrO_2, α-Al_2O_3, γ-Al_2O_3 and $BaTiO_3$ spheres, are shown in Figure S.5, Figure S.6, Figure S.7, Figure S.8 and Figure S.9, respectively. Only the -Al_2O_3 spheres show a type IV isotherm, indicating mesoporosity. The other materials do not have measurable porosity below 50 nm (i.e., the pore sizes that can be evaluated by nitrogen sorption).

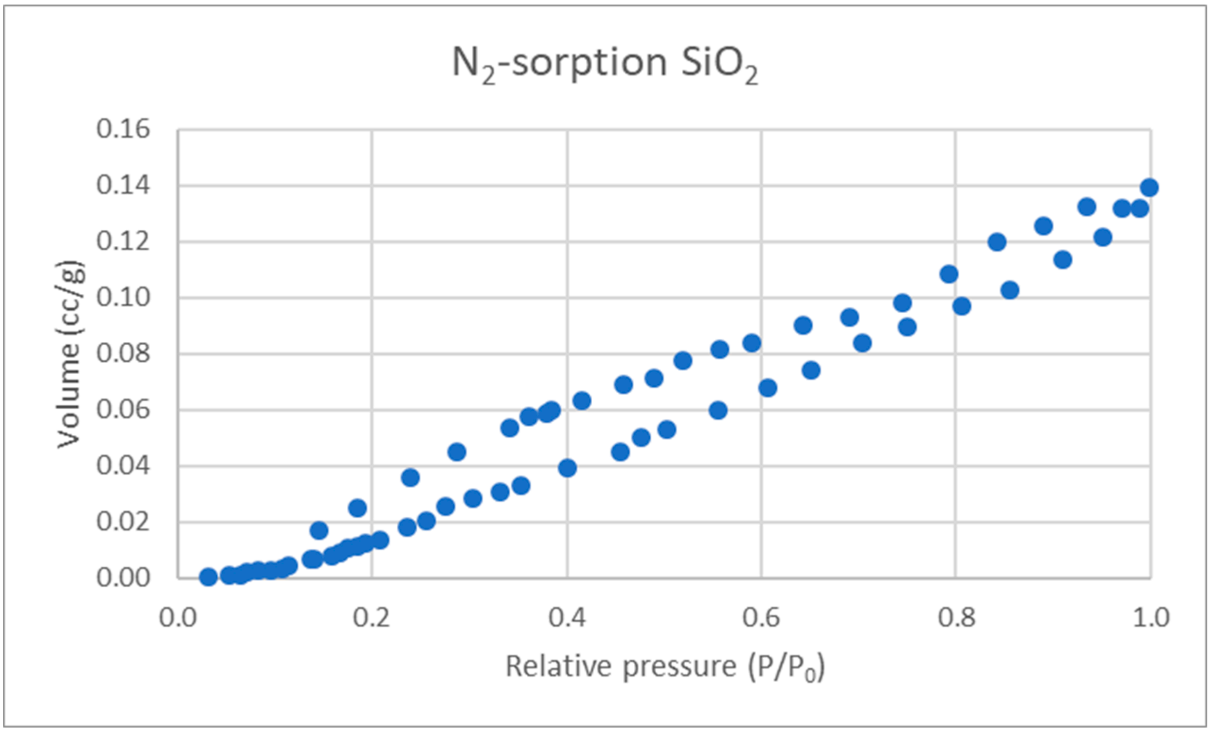

Figure S.5: Nitrogen Sorption for SiO_2

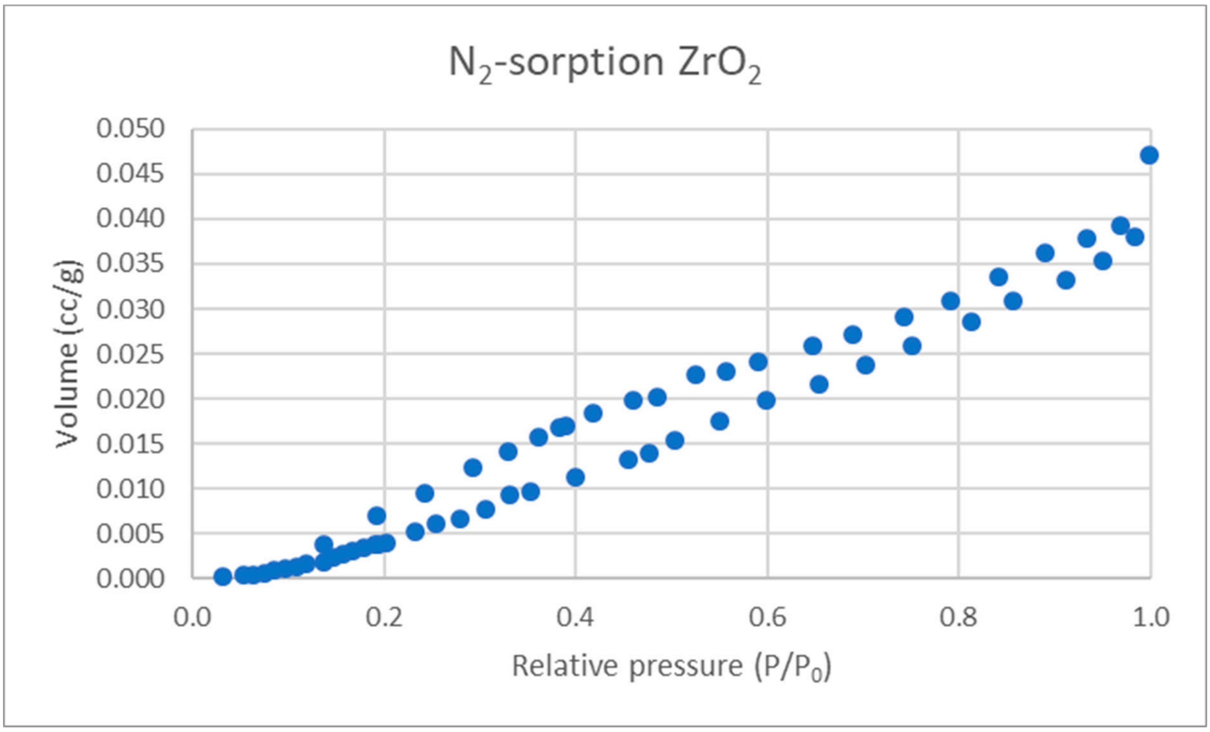

Figure S.6: Nitrogen Sorption for ZrO_2

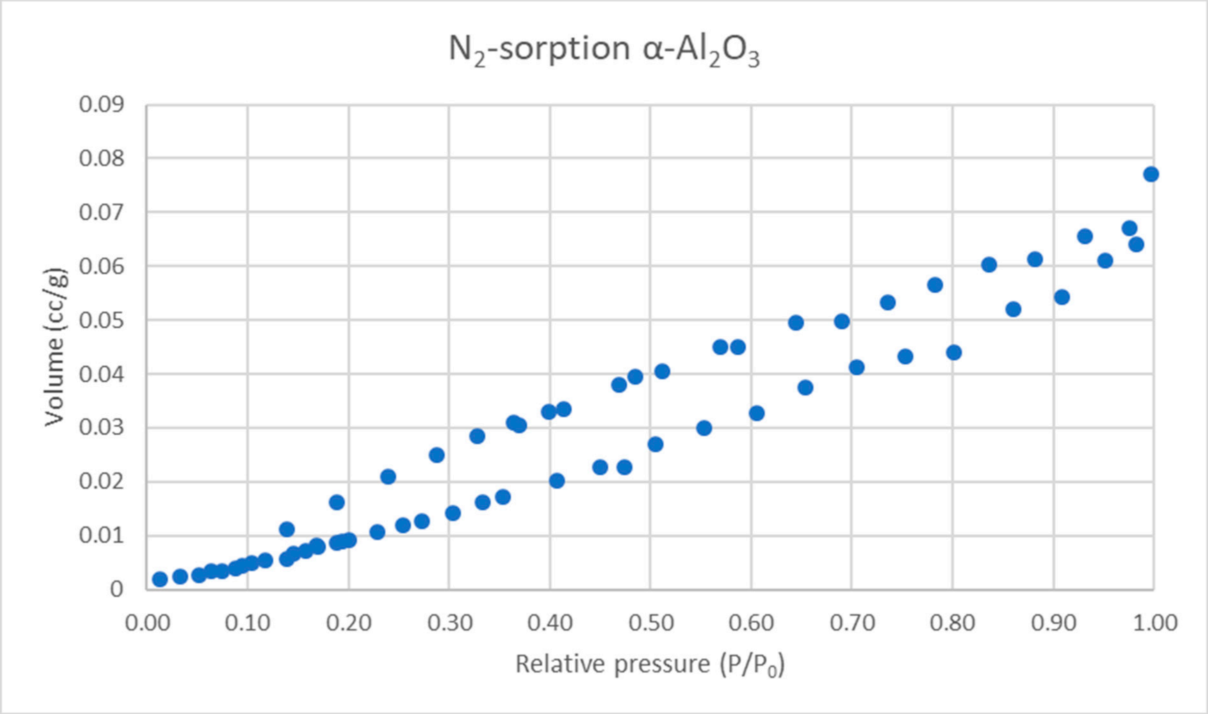

Figure S.7: Nitrogen Sorption for α-Al_2O_3

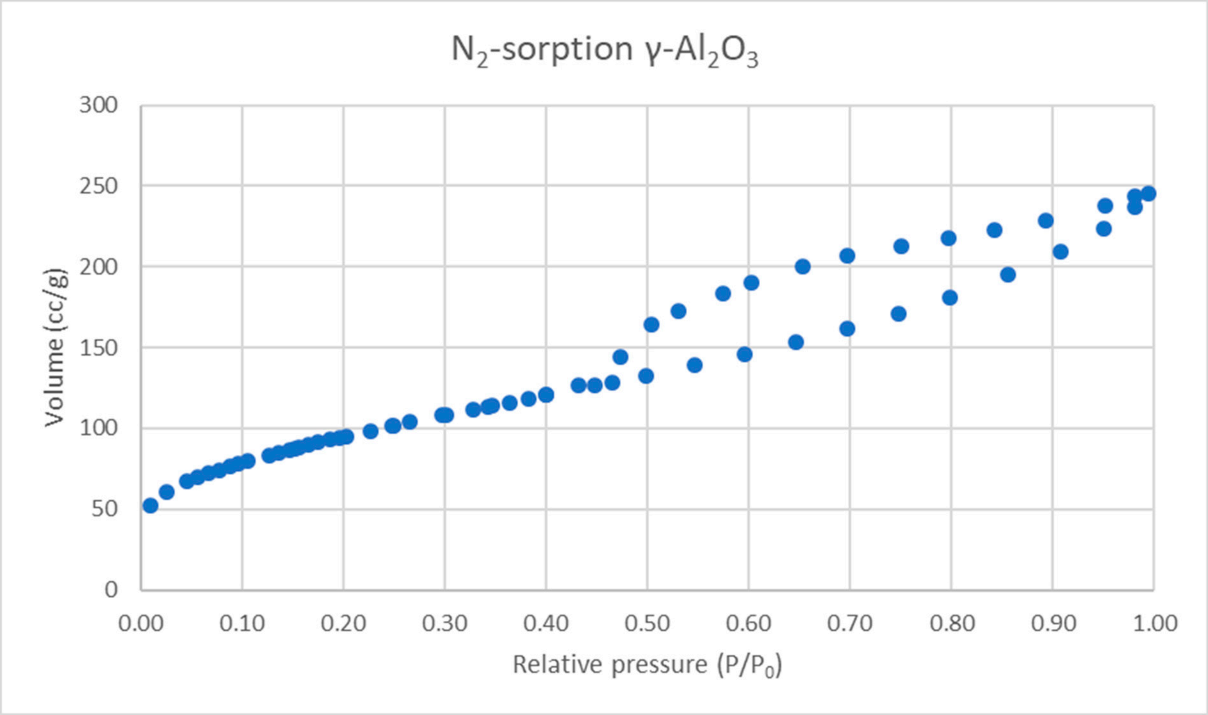

Figure S.8: Nitrogen Sorption for γ-Al_2O_3

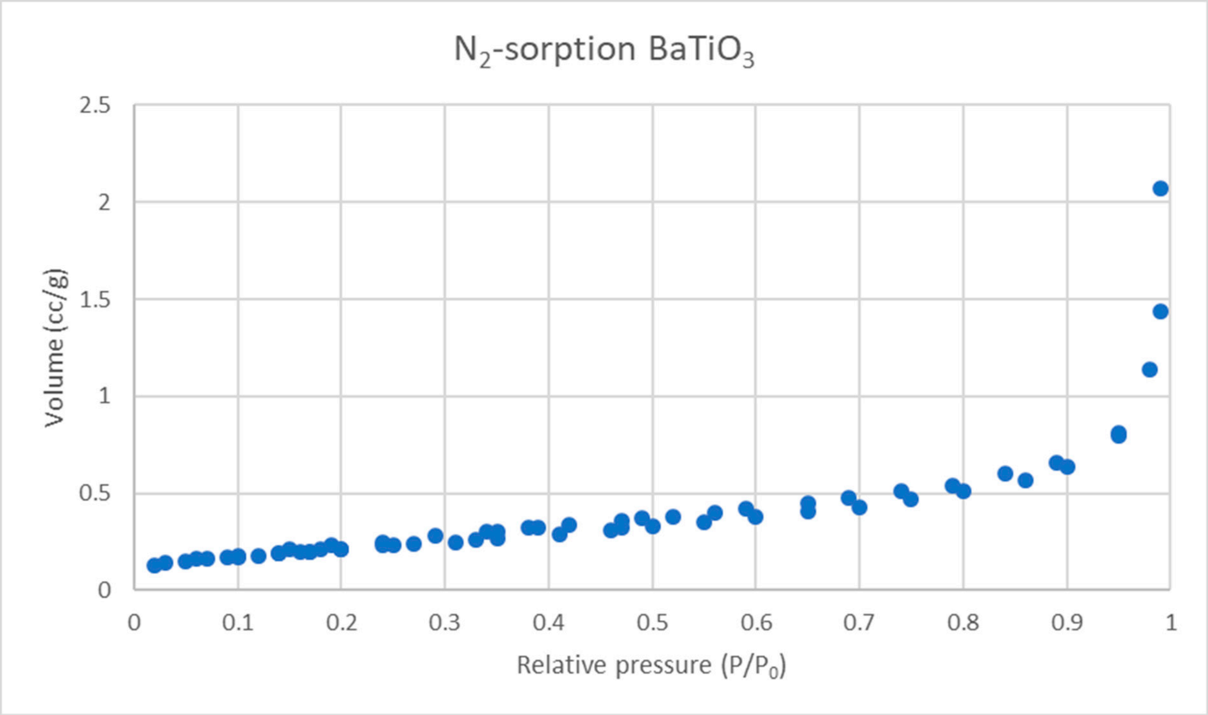

Figure S.9: Nitrogen Sorption for $BaTiO_3$

2.3 Hg-porosimetry

Figure S.10, Figure S.11, Figure S.12, Figure S.13 and Figure S.14 show the Hg-porosimetry results, able to detect porosity above 8 nm up to micrometre sized micropores. Pore sizes and the total open pore volume of the SiO_2, ZrO_2, α-Al_2O_3, γ-Al_2O_3 and $BaTiO_3$ spheres are shown, respectively. The most important data for these figures (the total open pore volume and the pore size) are shown in Table S.1. Moreover, it is clear that all samples have a (limited) macroporosity (>0.05 μm), but the amount of macropores and their size depend on the material.

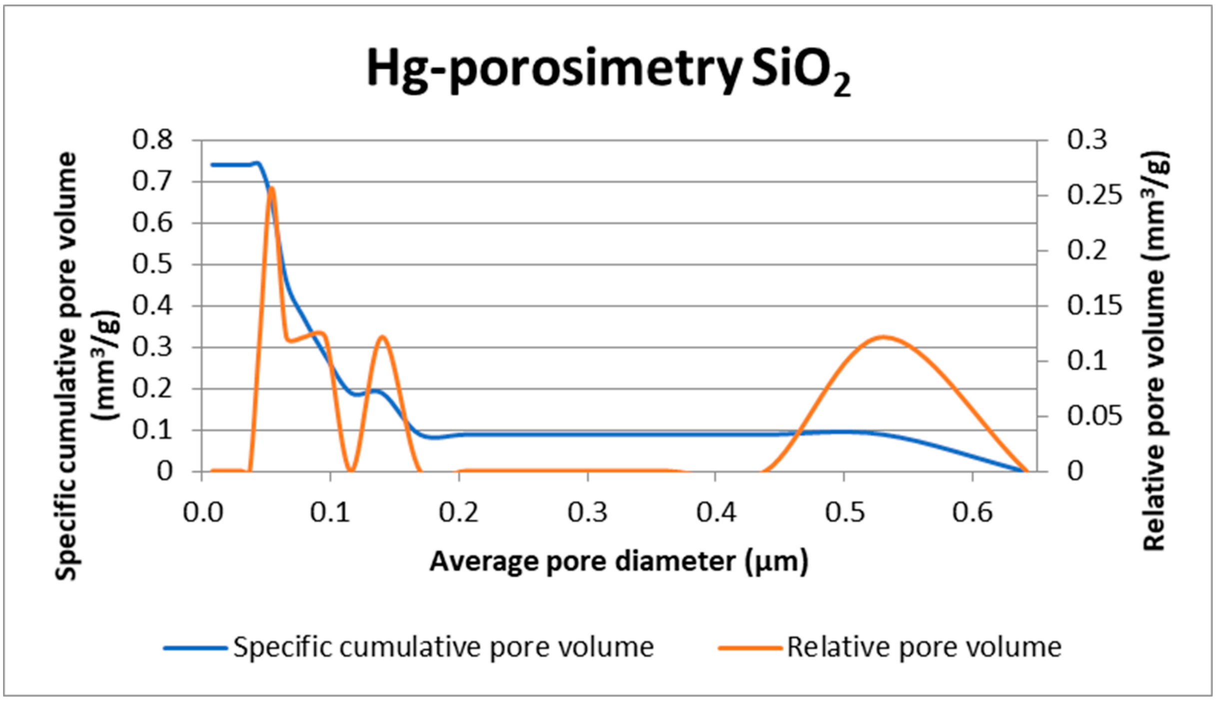

Figure S.10: Hg-porosimetry for SiO_2

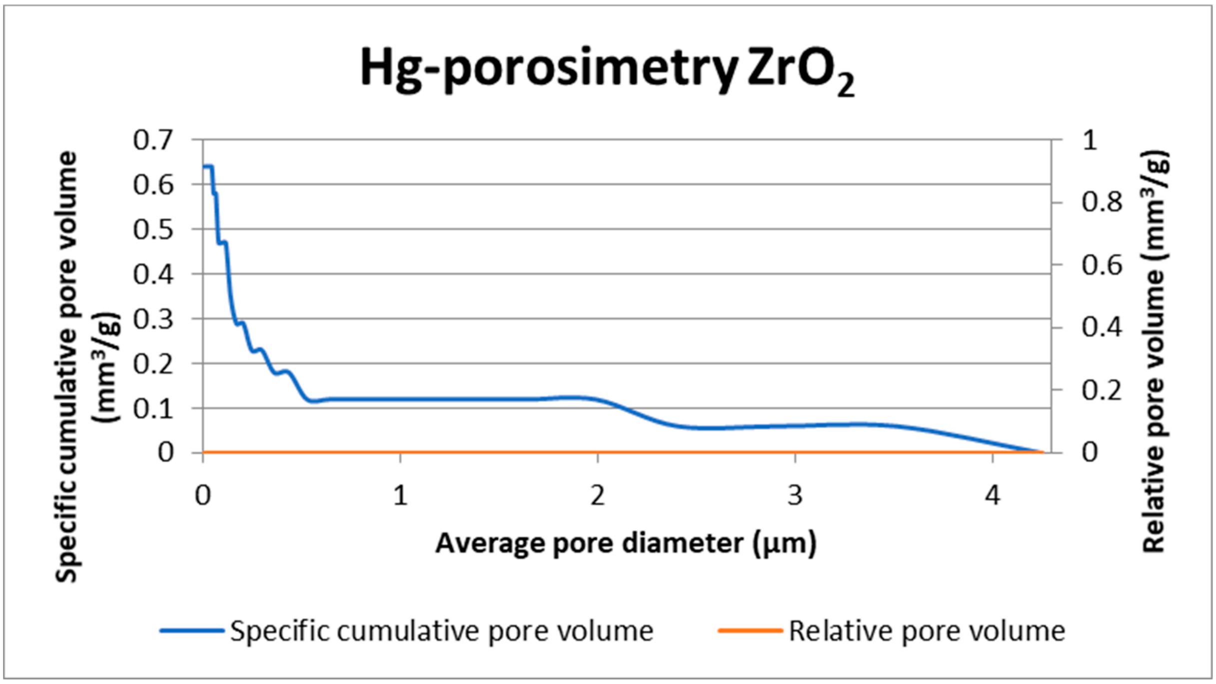

Figure S.11: Hg-porosimetry for ZrO_2

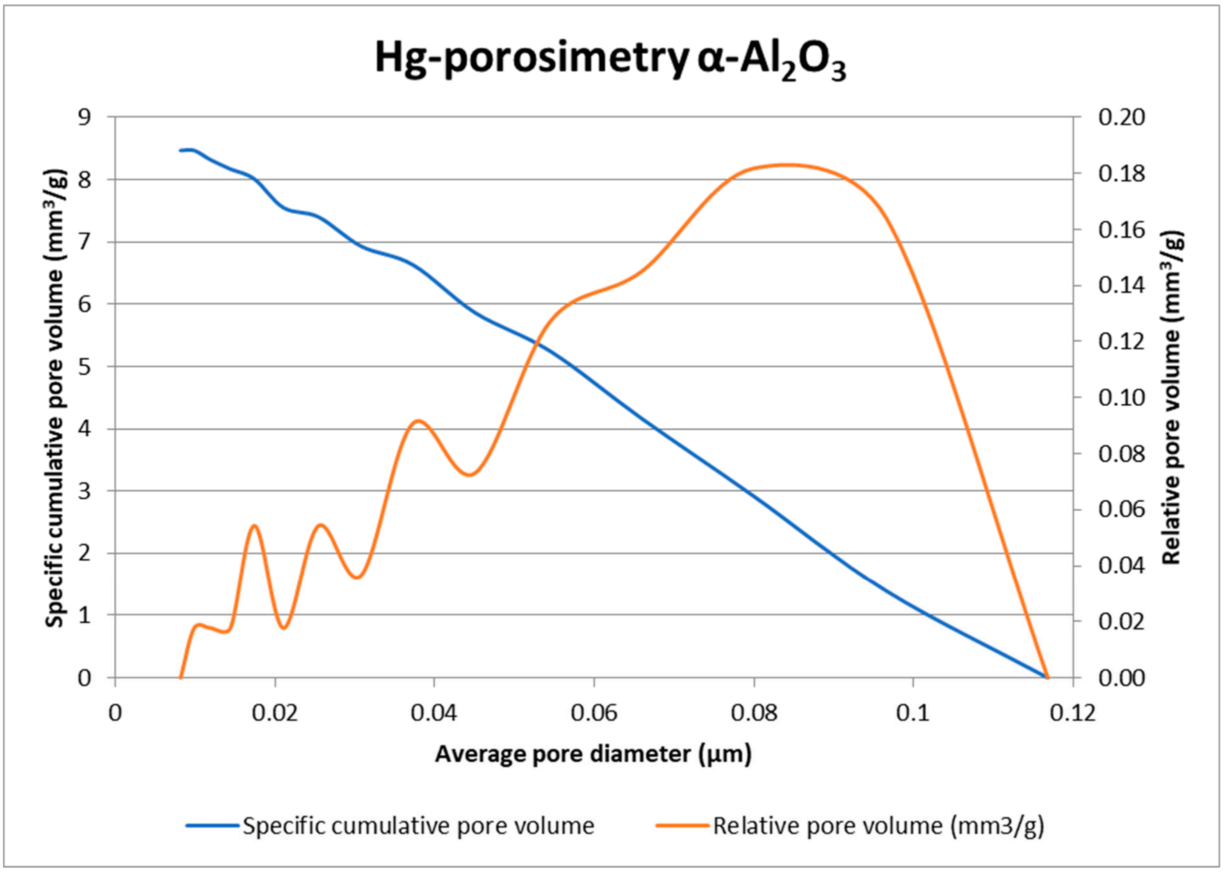

Figure S.12: Hg-porosimetry α-Al_2O_3

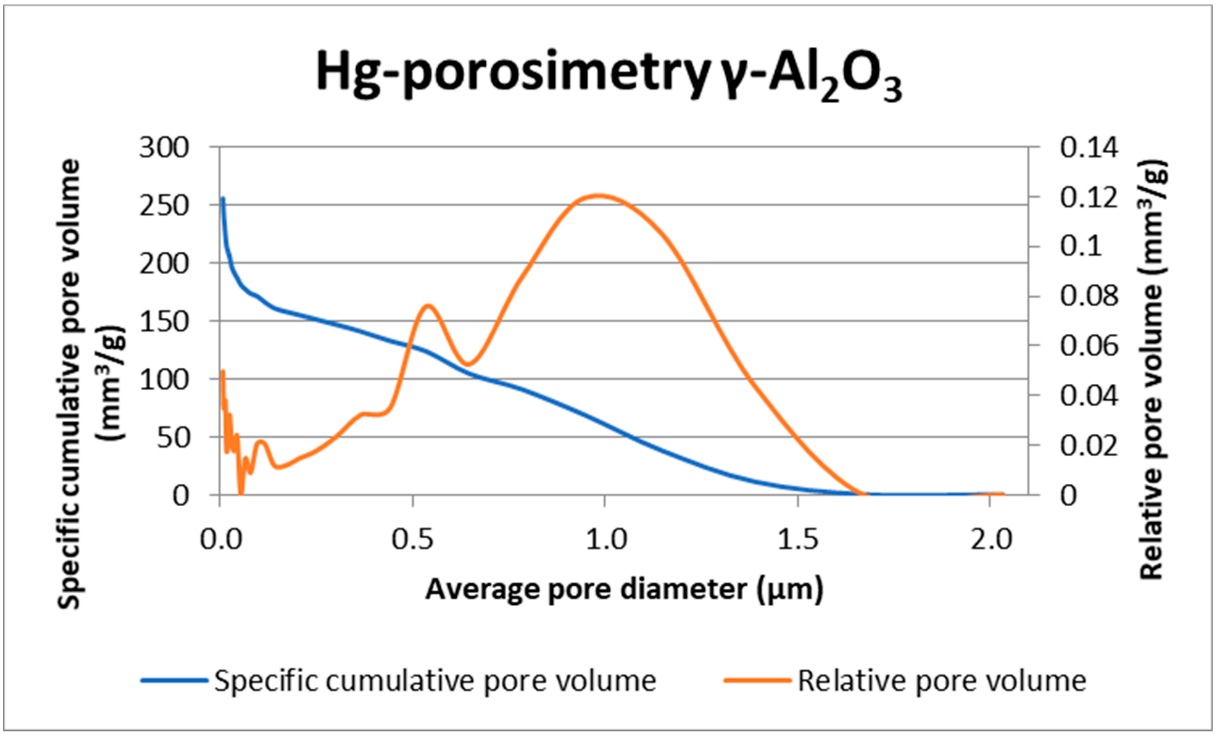

Figure S.13: Hg-porosimetry γ-Al_2O_3

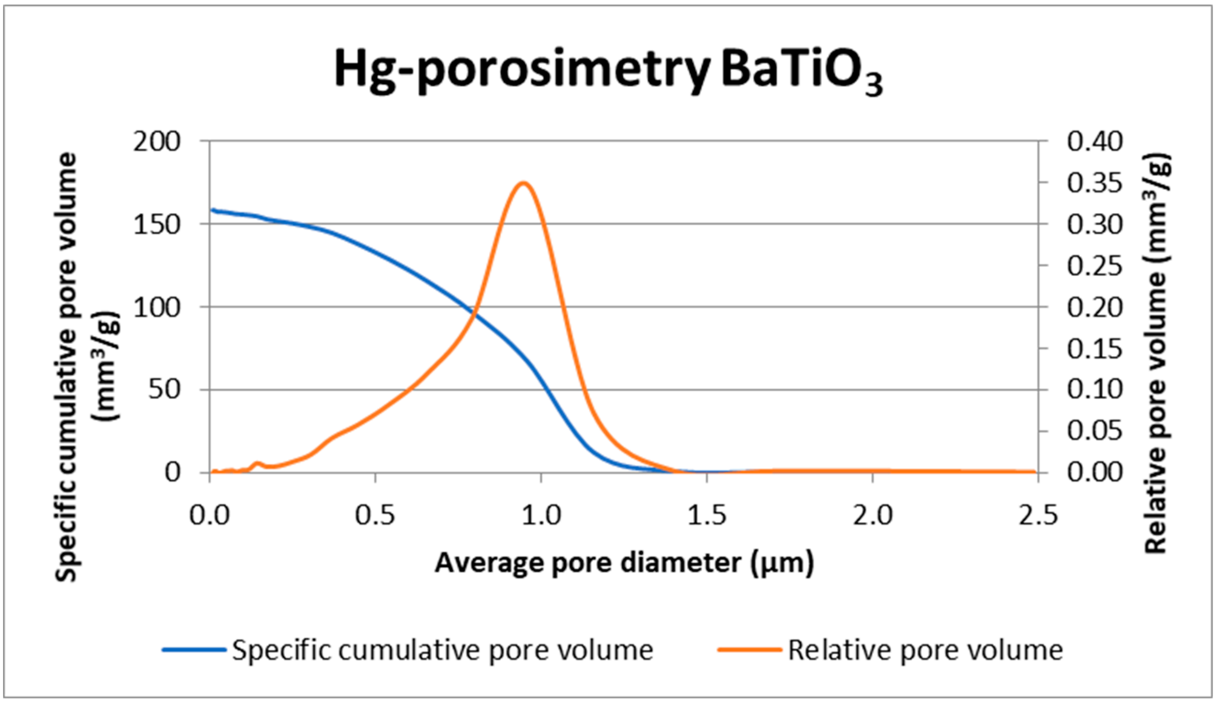

Figure S.14: Hg-porosimetry $BaTiO_3$

2.4 SEM EDX

Table S.4: SEM-EDX measurements for all spheres before and after plasma, measured at 3 points per sphere.

	SiO_2		**ZrO_2**		**α-Al_2O_3**		**γ-Al_2O_3**		**$BaTiO_3$**	
	Before plasma	After plasma	Before plasma	After plasma	Before plasma	After plasma	Before plasma	After plasma	Before plasma	After plasma
	Weight%	Weight%	Weight%	Weight%	Weight%	Weight%				
O	45.8±0.9	45.8±0.8	26.0±0.1	26.0±0.1	49±4	47±0.1	47±0	47±0	20.8±0.2	20.7±0.1
Si	33±2	32±1					0.2±0	0.2±0		
Na	11±2	14±3								
Ca	8±4	5±1	0.2±0	0±0	0±0	0.2±0.1				
Mg	2.2±0.5	2.6±0.3								
Al	0.5±0.2	0.5±0.2	0.5±0.3	0.3±0.1	52±2	52.5±0.4	52.8±0	52.6±0.1	0.2±0	0±0
K	0.4±0	0.3±0.3								
Zr			71.5±0.2	72.5±0.2						
Hf			1.8±0.1	1.2±0.2						
Ba									58.4±0.6	58.7±0.1
Ti									20.7±0.4	20.7±0.1

The SEM-EDX data (Table S.4) of SiO_2, α-Al_2O_3, γ-Al_2O_3 and $BaTiO_3$ show no significant difference when analysing the spheres before and after plasma. When comparing the results for ZrO_2, we can see that the content of Ca and Hf decreases after plasma exposure, but the deviation is minimal. Therefore, no conclusions can be drawn based on these measurements.

3. GAS CHROMATOGRAM

Figure S.15 shows an example of a chromatogram obtained from an experiment with the non-packed reactor at 50ml/min. It is shown to aid with the estimation of the abundancy of the components that were not identified/calibrated in the GC and thus could be the cause for the missing percentages in the carbon, hydrogen and oxygen balance.

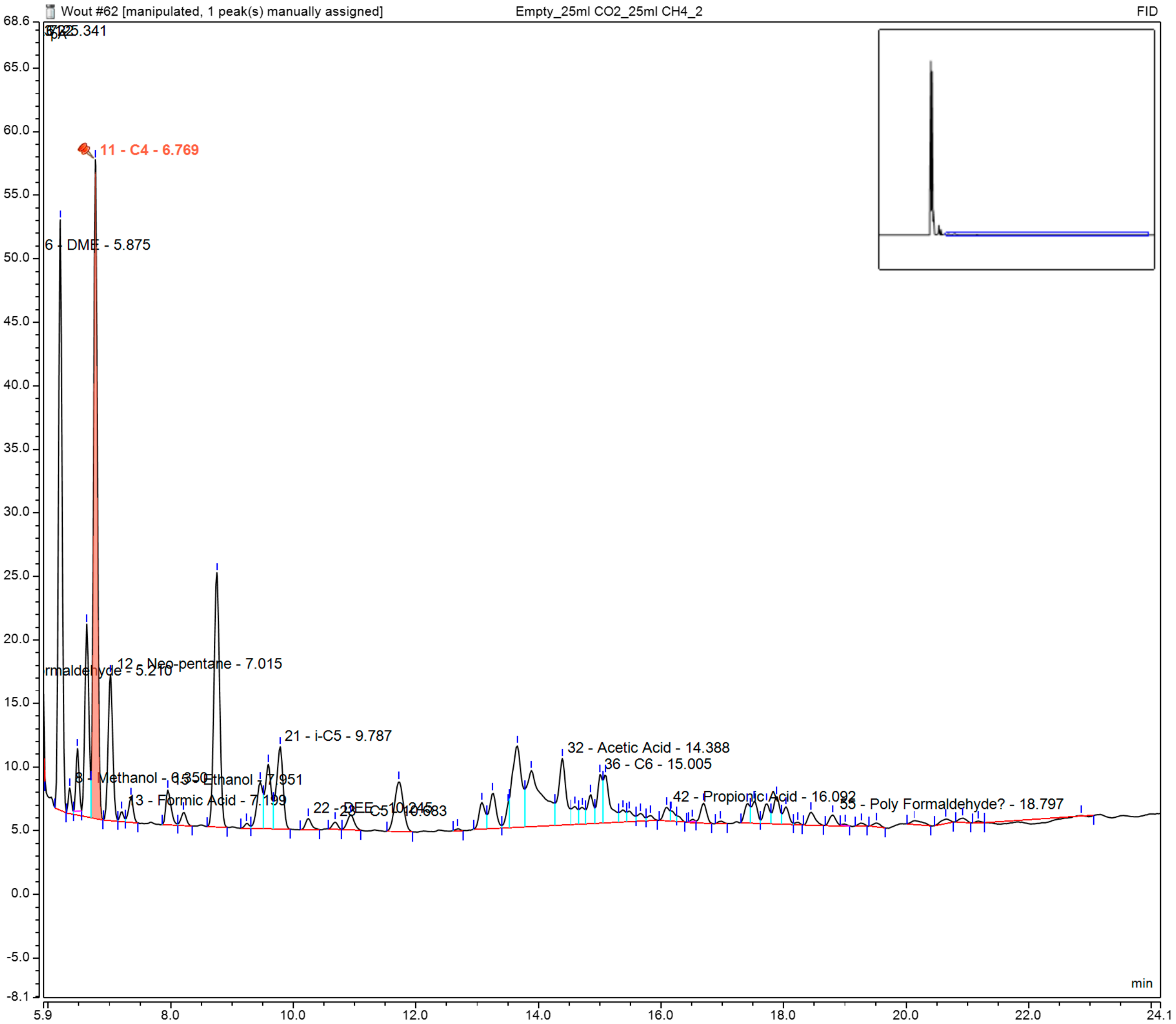

Figure S.15: Part of a gas chromatogram obtained in this work, zoomed in on the baseline.

4. MATERIAL STABILITY AGAINST COKING

None of the samples showed weight loss in TGA (performed up to 800 ºC, so above the decoking temperature [15]). This indicates the limited amount of coke formation, which confirms the literature that the plasma process will induce less coking than thermal DRM [16]. Nevertheless, there are some coloured (black) spots when the packing is removed from the reactor, hence a more detailed analysis via Raman microscopy has been done to determine its origin. This shows that some coking is still present. The measurements were performed with a Horiba Xplora Plus micro-Raman, with a 50x magnification and a wavelength of 532 nm. Clear signals of the D and G bands of carbon can be observed for the SiO_2 packing (Figure S.16) at 1330 cm^{-1} and 1595 cm^{-1}, including shoulders around 1472 cm^{-1} and 1221 cm^{-1}, as well as non-resolved overtone signals. When looking more closely to the -Al_2O_3 and ZrO_2 packing materials, unresolved broad signals can be observed in the region where also coke displays signals. However, as the signals are not resolved, it is difficult to confirm that this is due to some limited coke formation. Moreover, there was no detectable signal when measuring the sphere, focussing on a black spot. For all spheres, the Raman spectrum before and after plasma is shown, and for α-Al_2O_3, γ-Al_2O_3 and $BaTiO_3$, a second figure shows a zoomed-in frame, to better vision the coking regions.

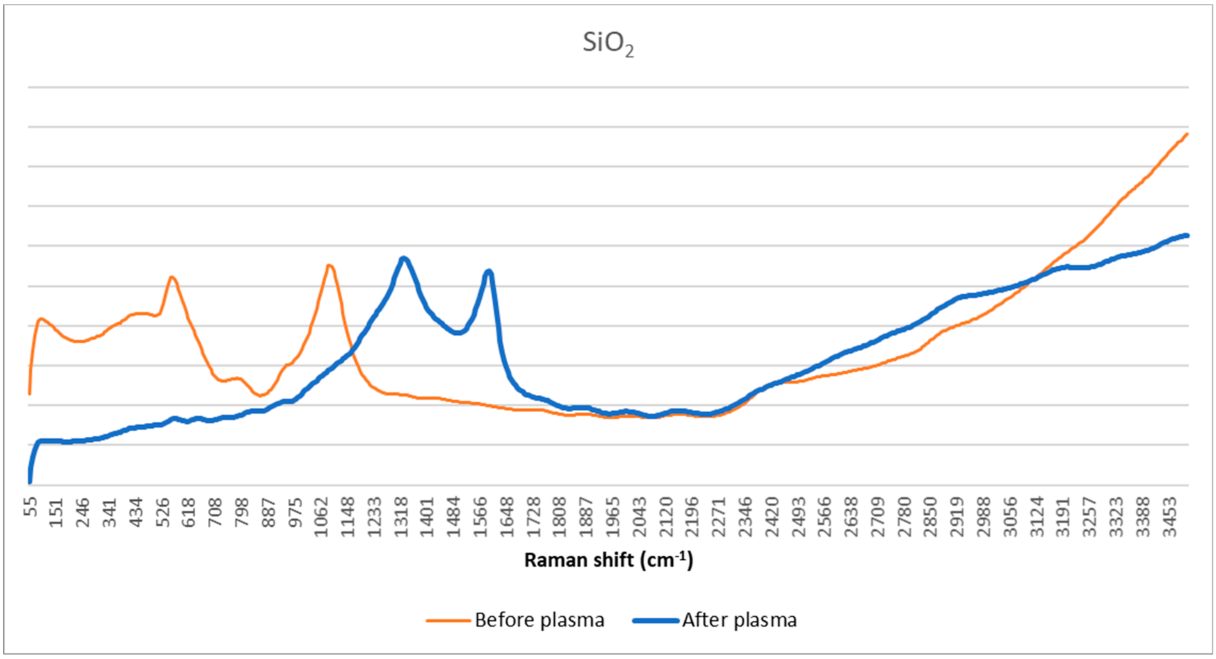

Figure S.16: Raman spectrum for SiO_2, before and after plasma exposure.

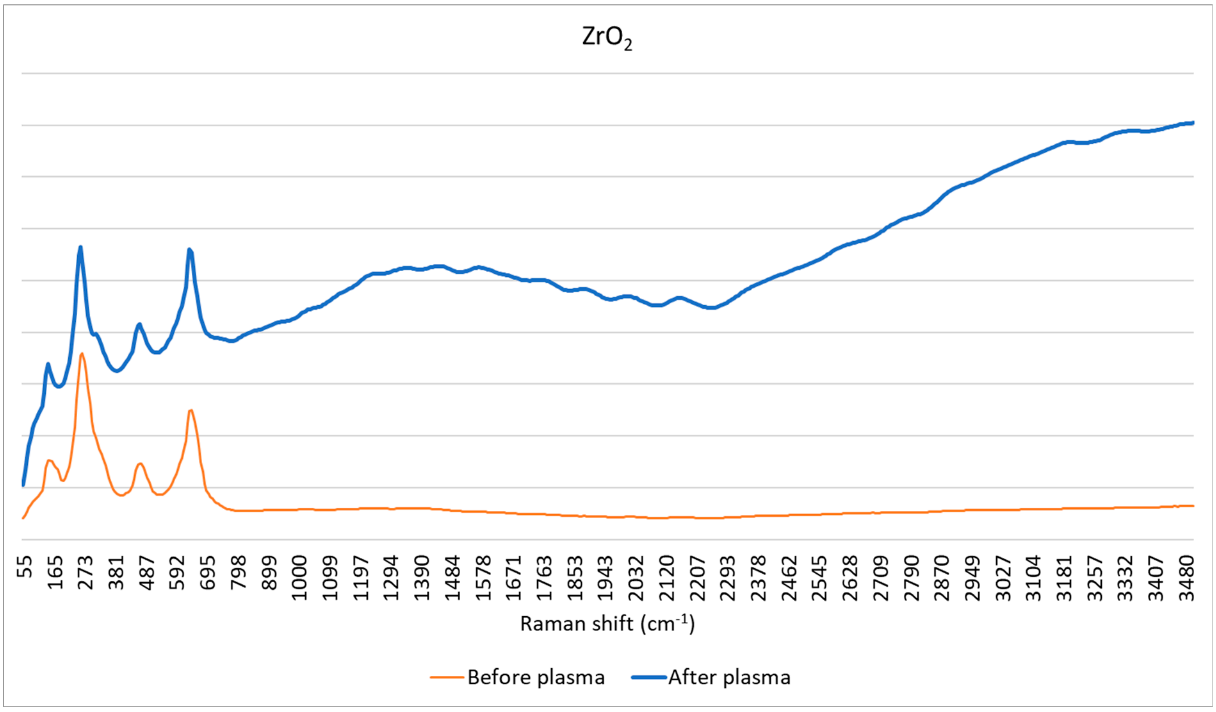

Figure S.17: Raman spectrum for ZrO_2, before and after plasma exposure.

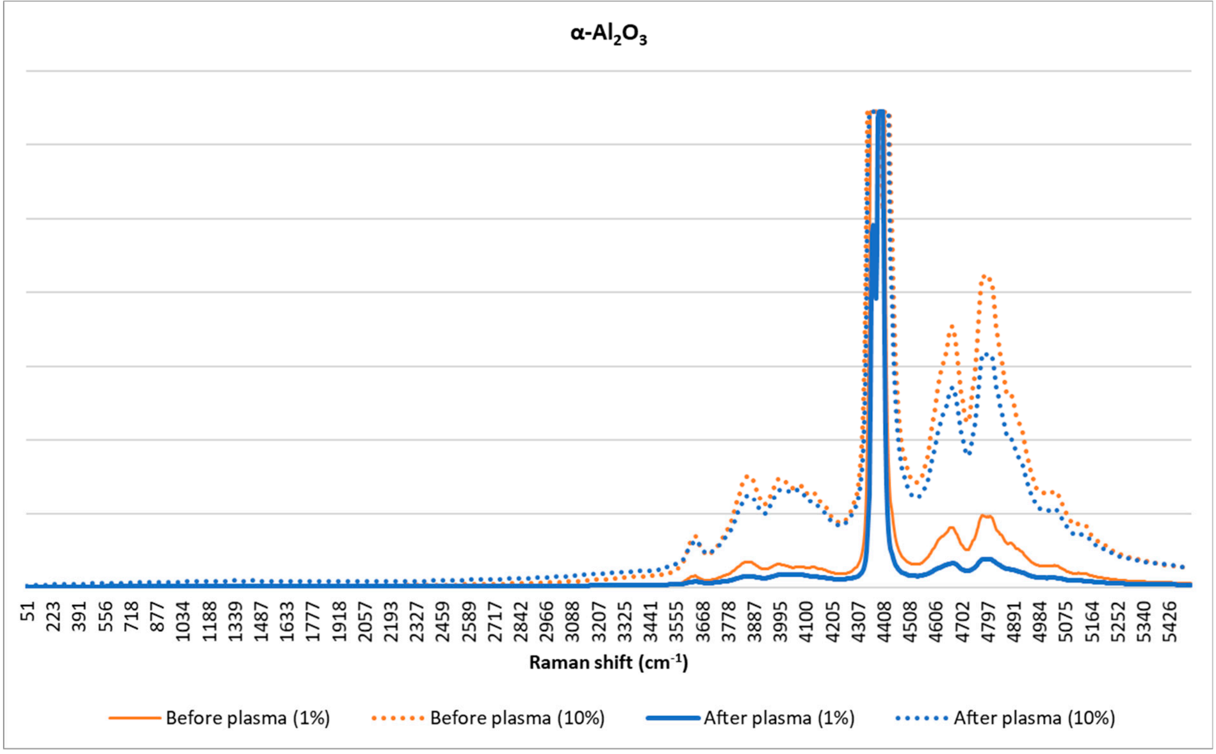

Figure S.18: Raman spectrum for α-Al_2O_3, before and after plasma exposure. For both spheres (before and after plasma), 2 spectra are recorded: one with 90% of the light filtered out, and one with 99% of the light filtered out.

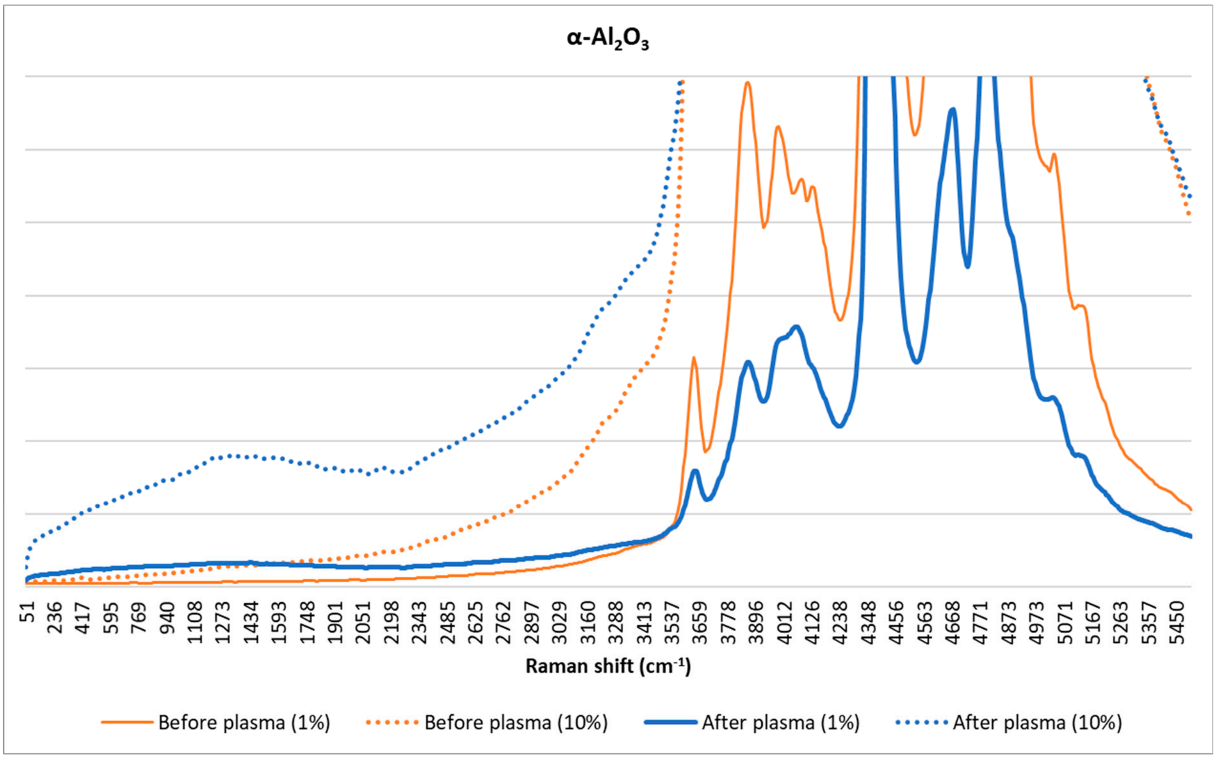

Figure S.19: Zoomed-in (at coking regions) Raman spectrum for α-Al$_2$O$_3$, before and after plasma exposure. For both spheres (before and after plasma), 2 spectra are recorded: one with 90% of the light filtered out, and one with 99% of the light filtered out.

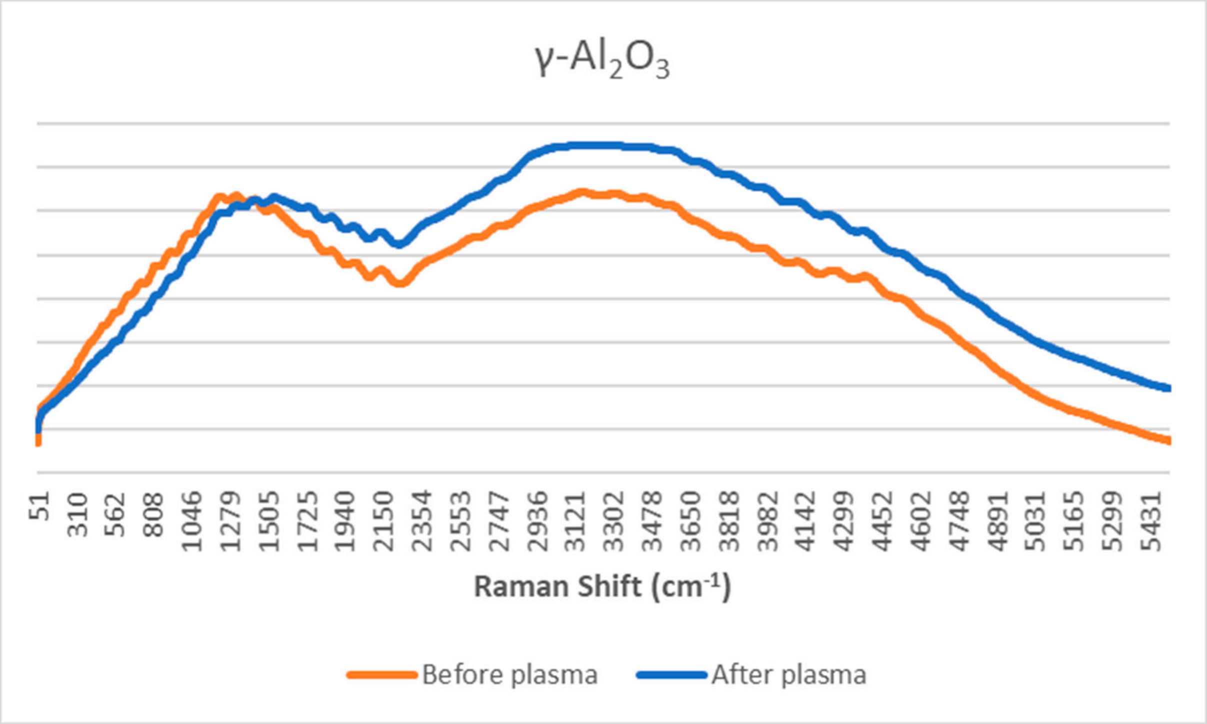

Figure S.20: Raman spectrum for γ-Al$_2$O$_3$, before and after plasma exposure.

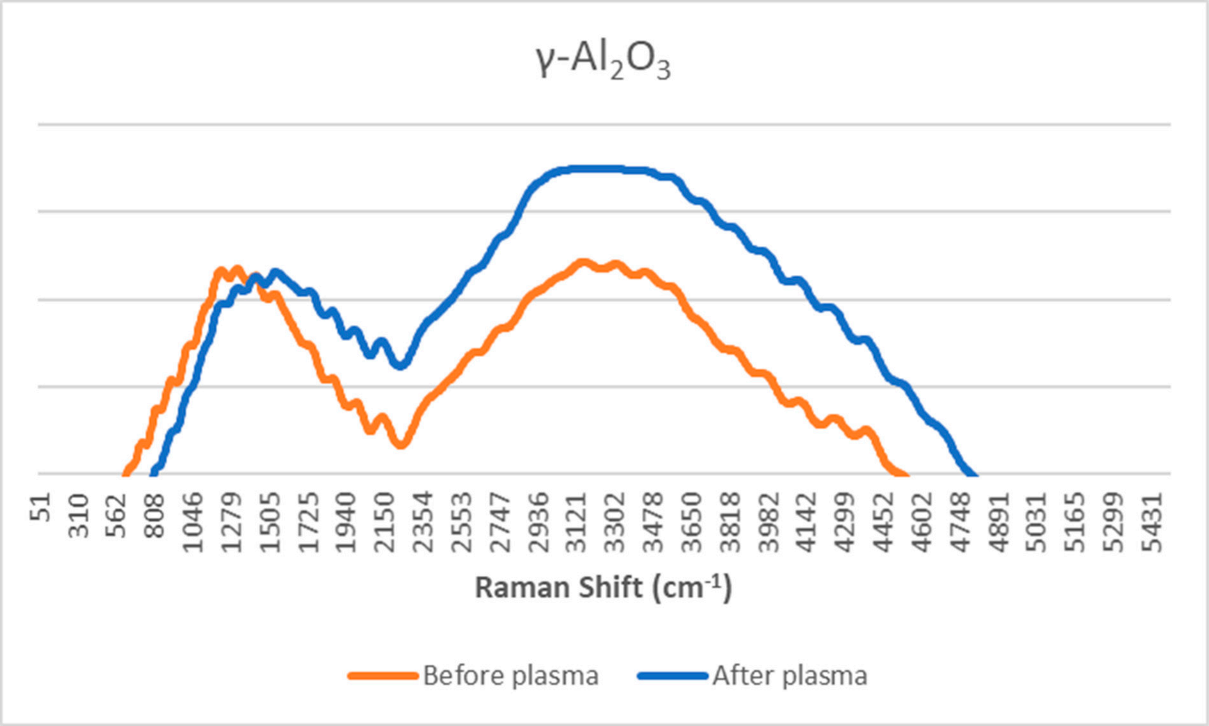

Figure S.21: Zoomed-in (at coking regions) Raman spectrum for γ-Al_2O_3, before and after plasma exposure

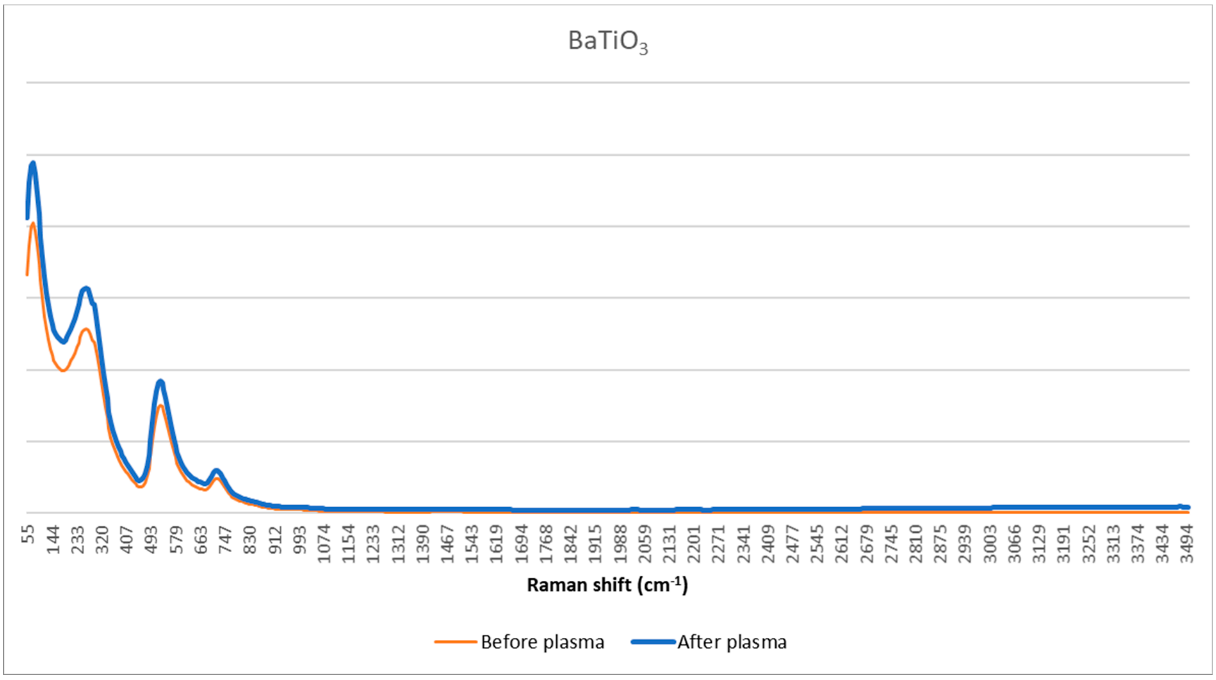

Figure S.22: Raman spectrum for $BaTiO_3$, before and after plasma exposure

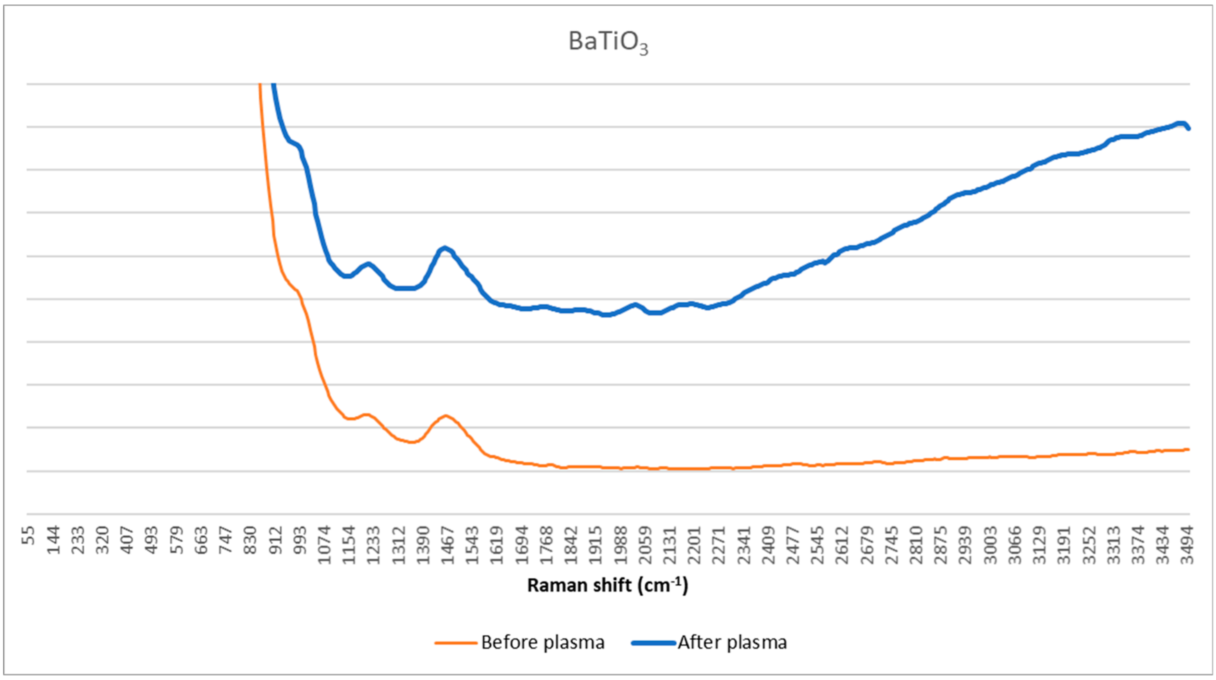

Figure S.23: Zoomed-in (at coking regions) Raman spectrum for BaTiO$_3$, before and after plasma exposure

Before plasma	After plasma
SiO$_2$	
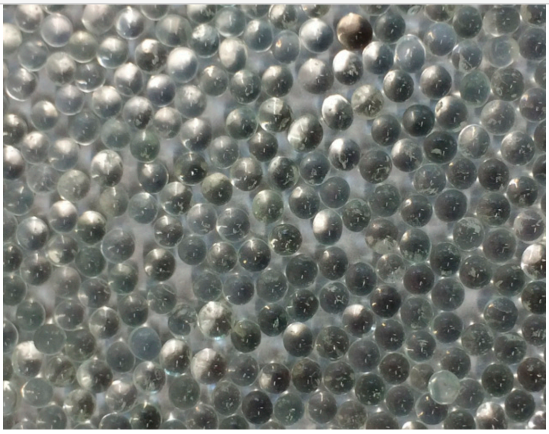	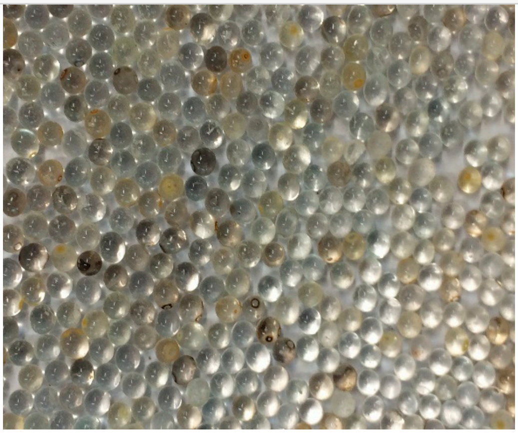
ZrO$_2$	

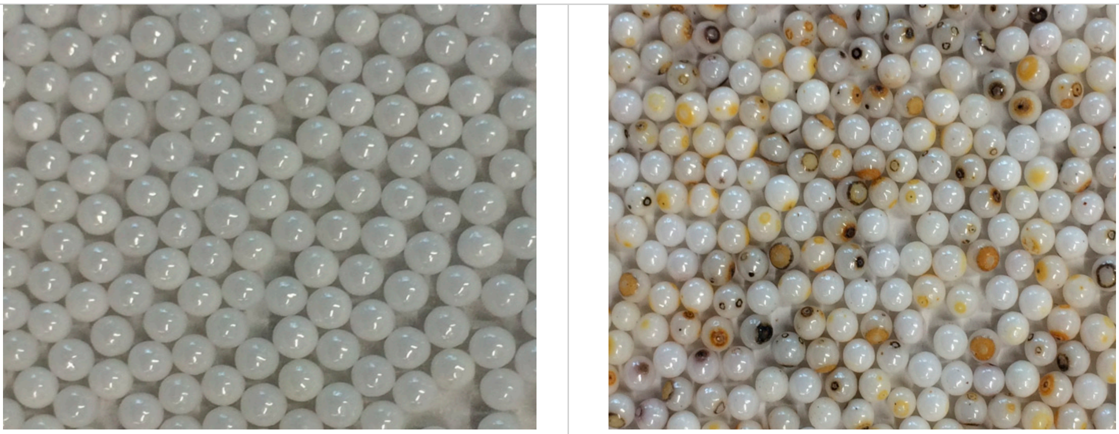

α-Al_2O_3

γ-Al_2O_3

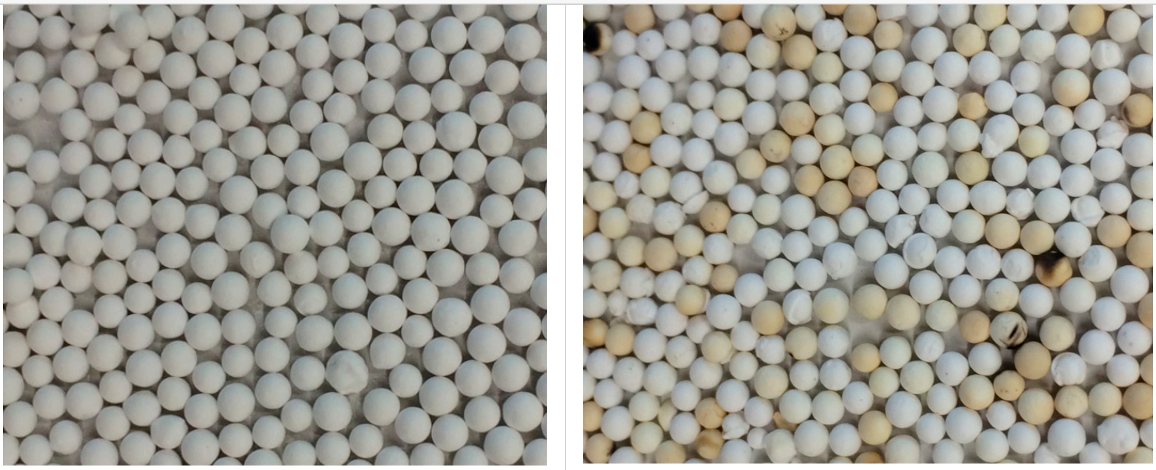

$BaTiO_3$

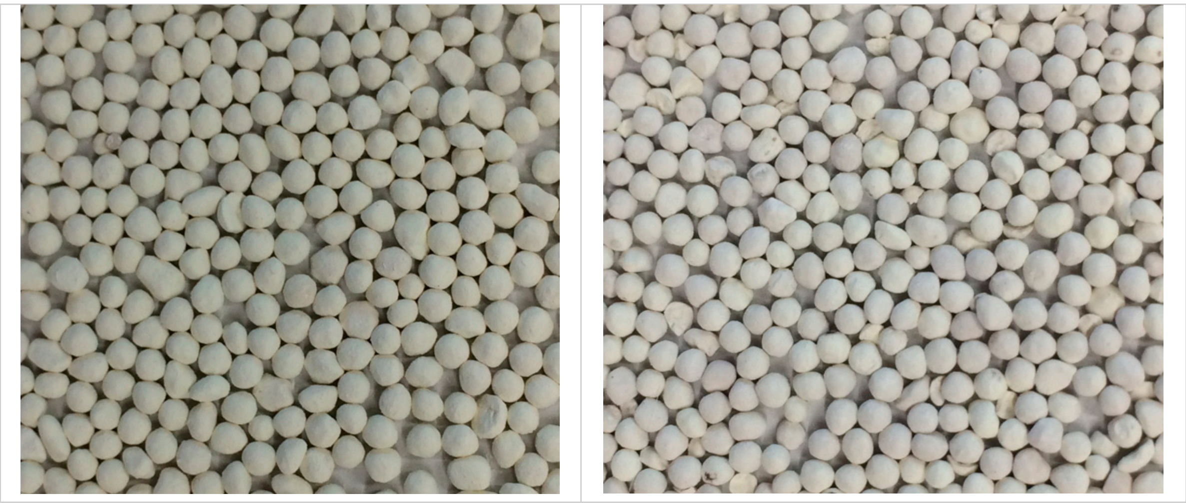

Figure S.24: visual image of the spheres before and after plasma treatment.

5. DETAILED CARBON, HYDROGEN AND OXYGEN BALANCES

First, for each element (carbon, hydrogen, oxygen) a complete balance is shown, with a detailed contribution of each component (figures: “total balance”). Then, to ensure better visibility, the same values were plotted, without the presence of the non-converted feed components (CO_2 and CH_4) (figures: “detailed balance”). Finally, a figure is shown with the same values as in the latter figure, but normalised to 100%.

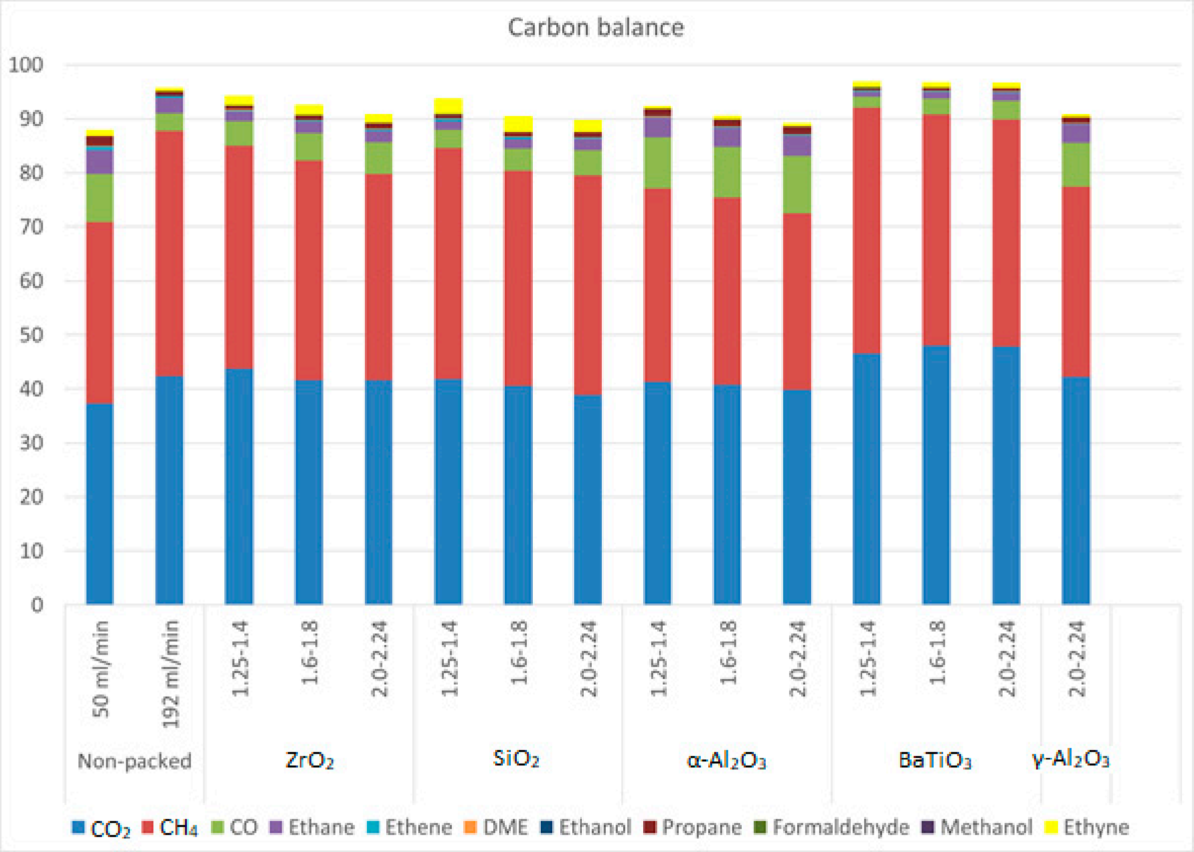

Figure S.25: Total carbon balance for different sphere sizes and materials.

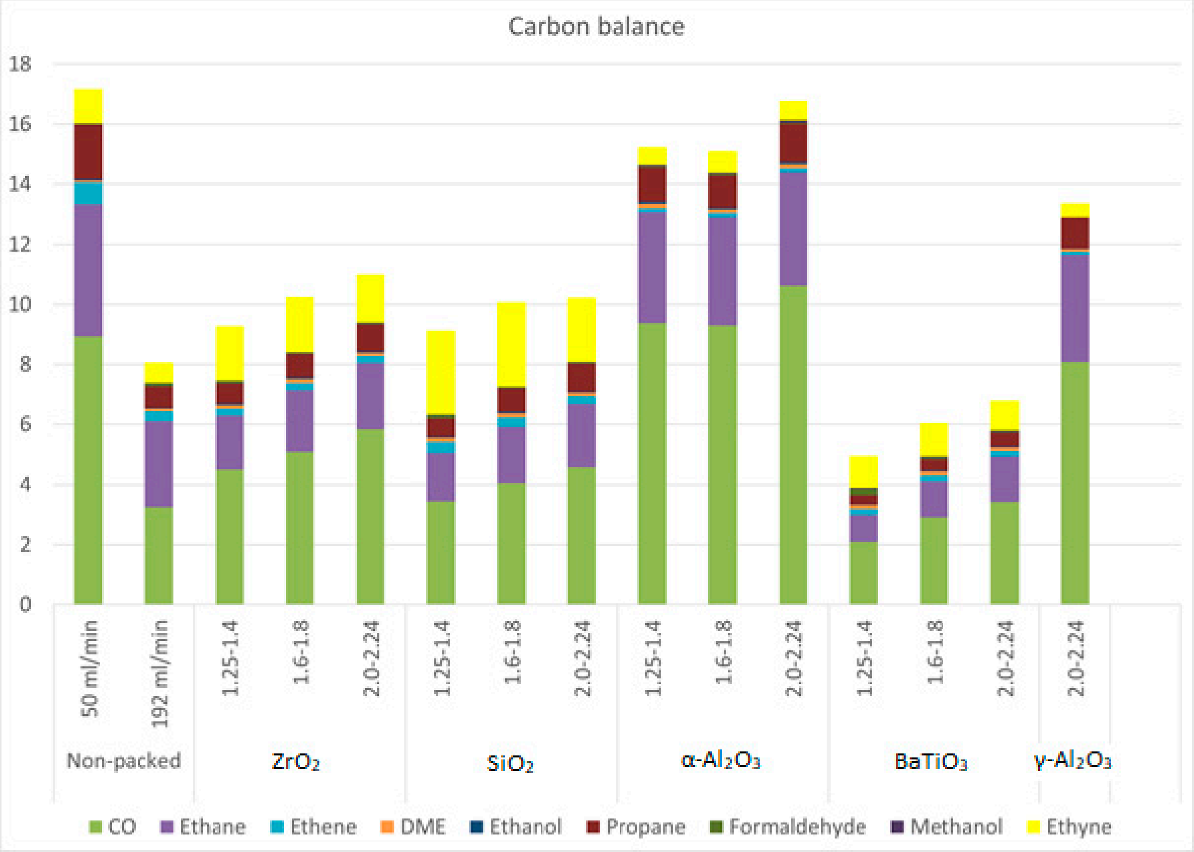

Figure S.26: Detailed carbon balance for different sphere sizes and materials, without CO_2 and CH_4 contribution.

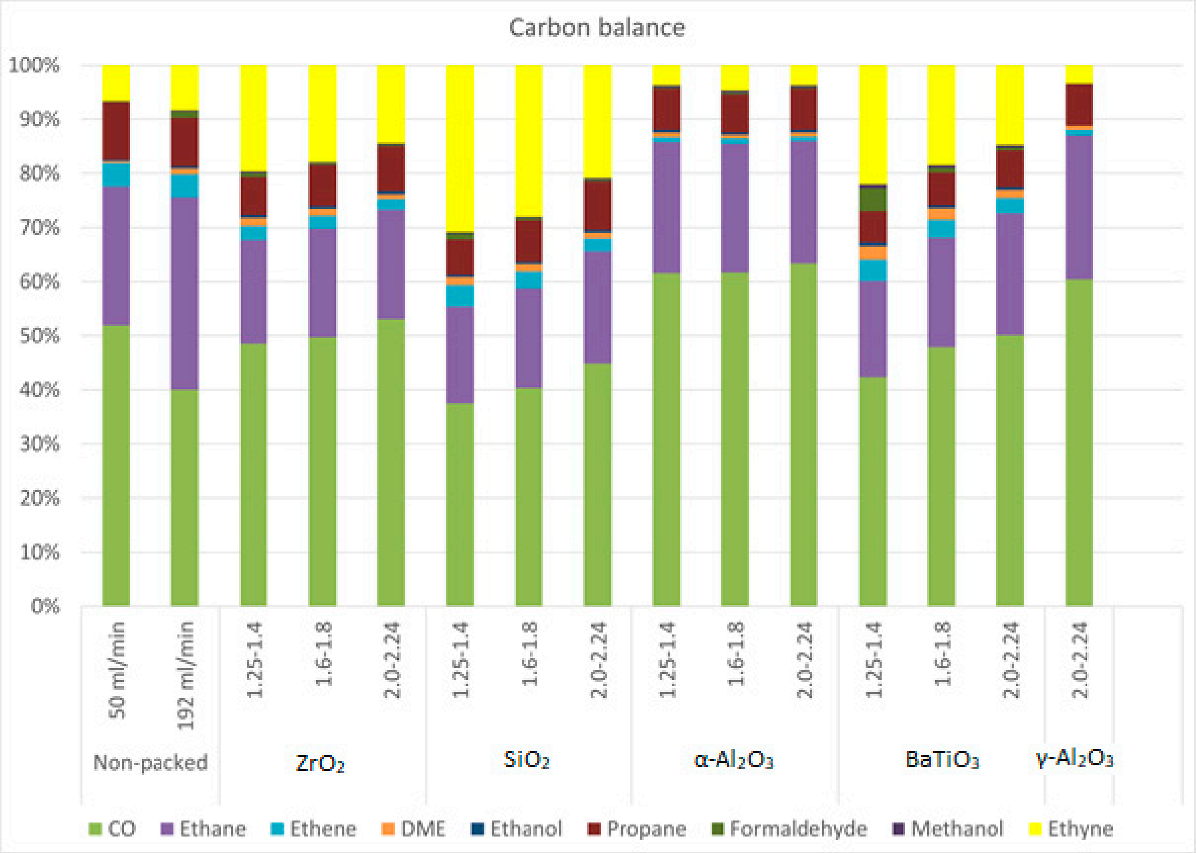

Figure S.27: Normalized carbon balance for different sphere sizes and materials, without CO_2 and CH_4 contribution.

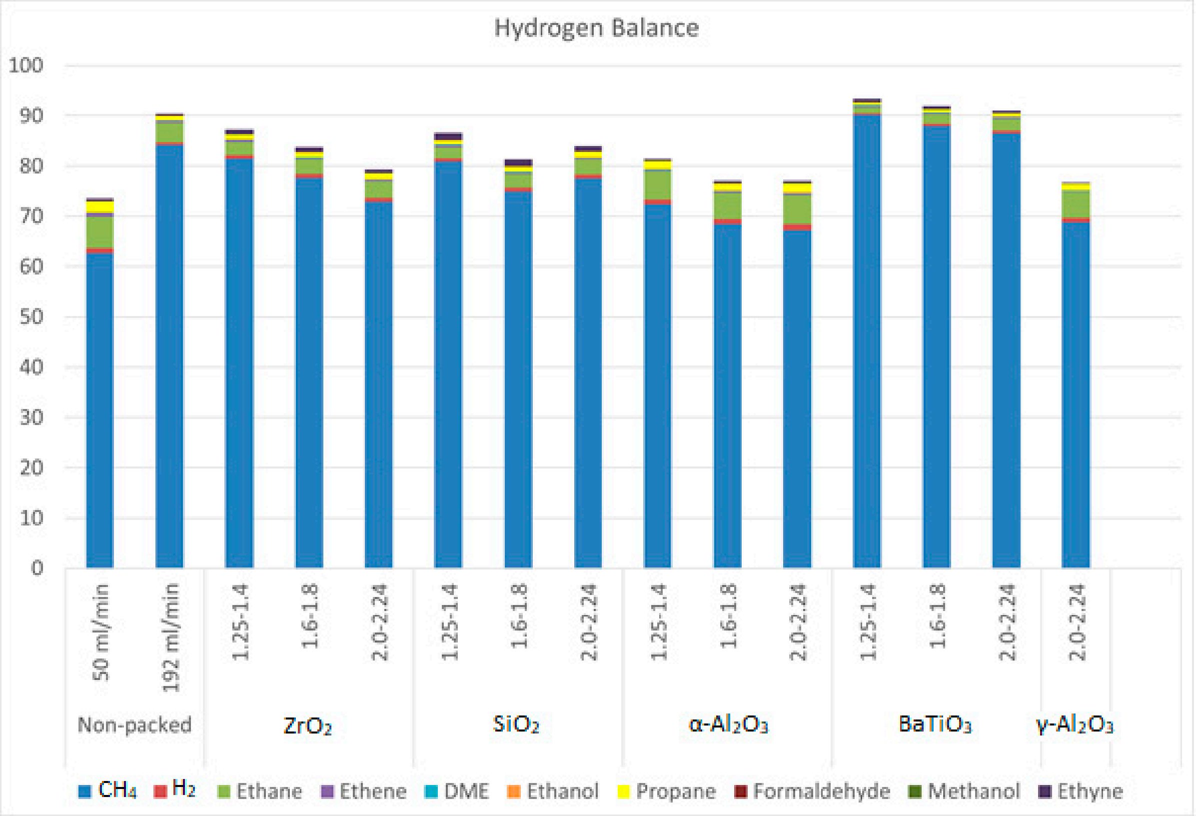

Figure S.28: Total hydrogen balance for different sphere sizes and materials

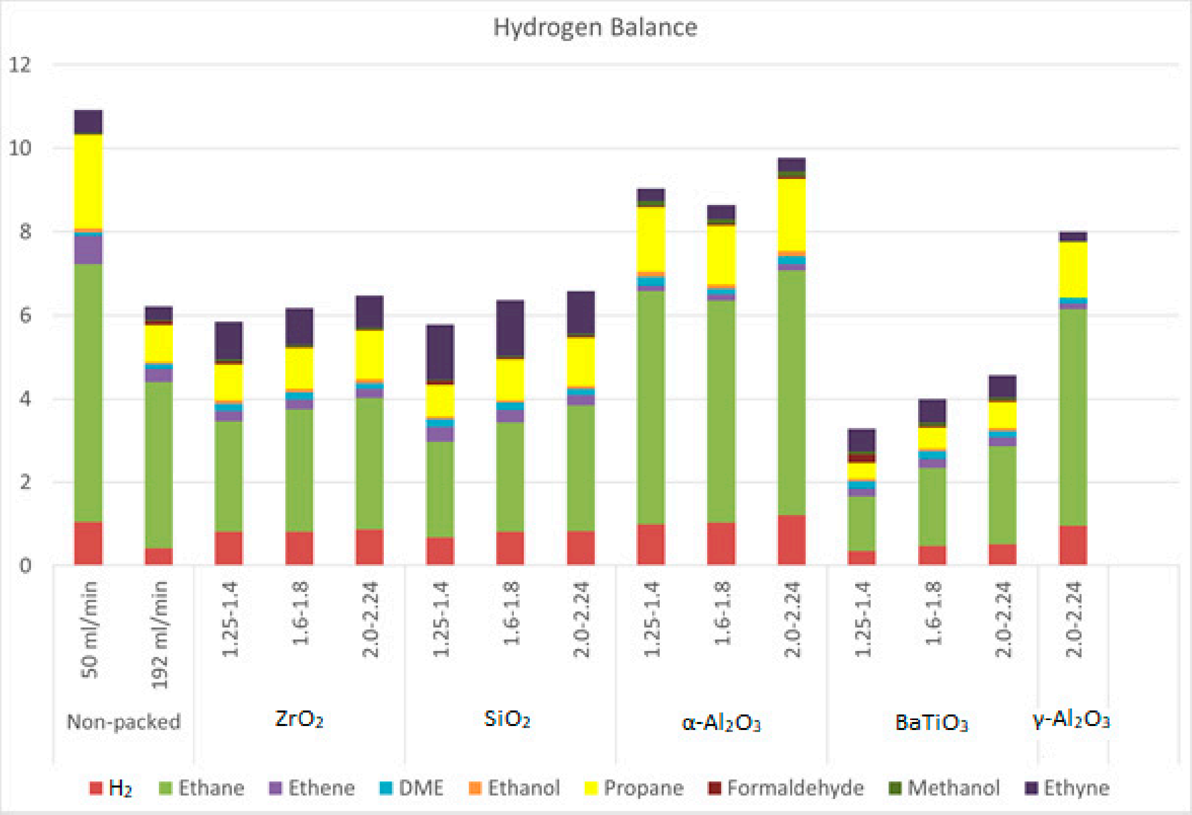

Figure S.29: Detailed hydrogen balance for different sphere sizes and materials, without CH_4 contribution

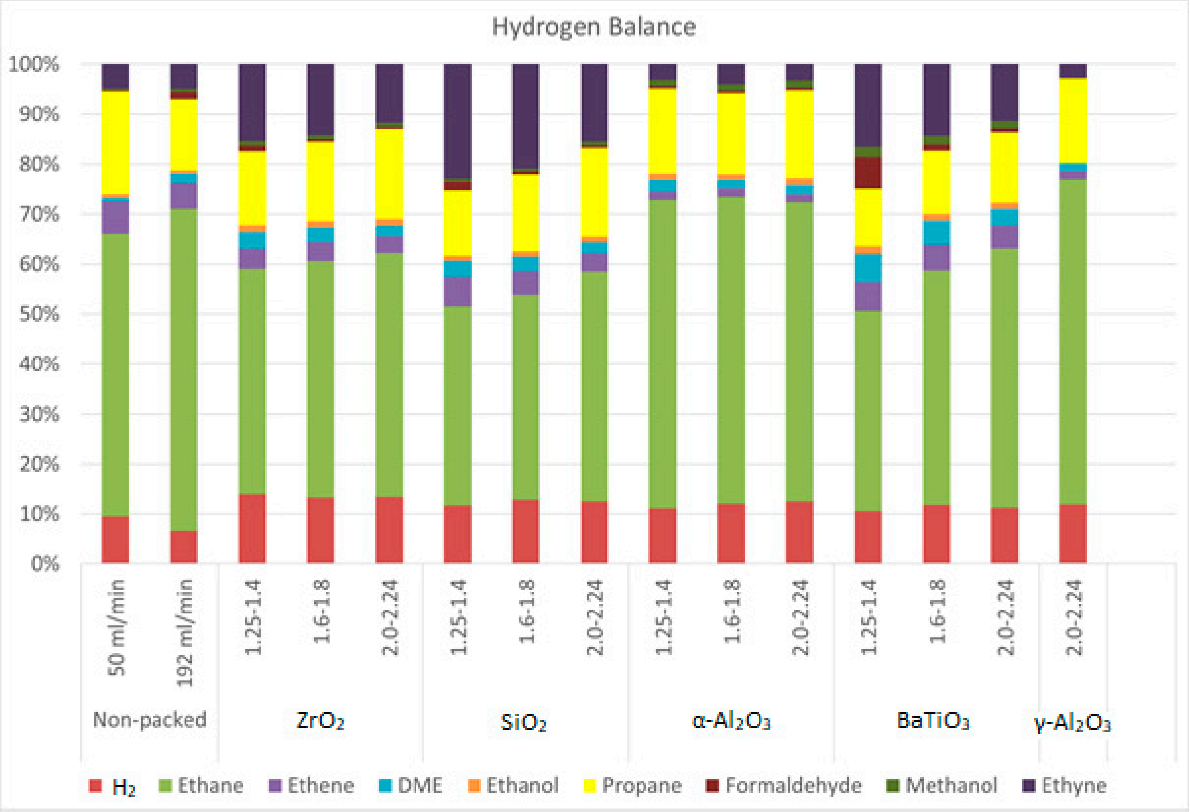

Figure S.30: Normalized hydrogen balance for different sphere sizes and materials, without CH_4 contribution

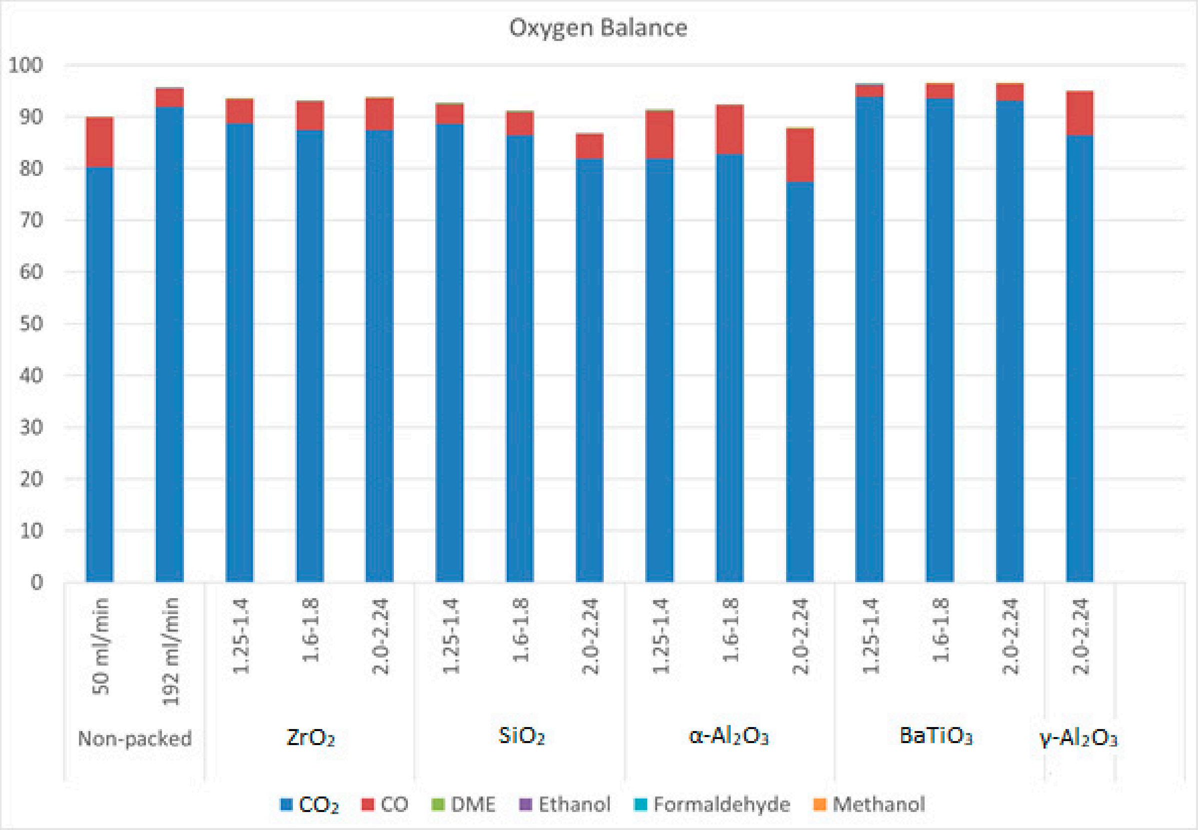

Figure S.31: Total oxygen balance for different sphere sizes and materials

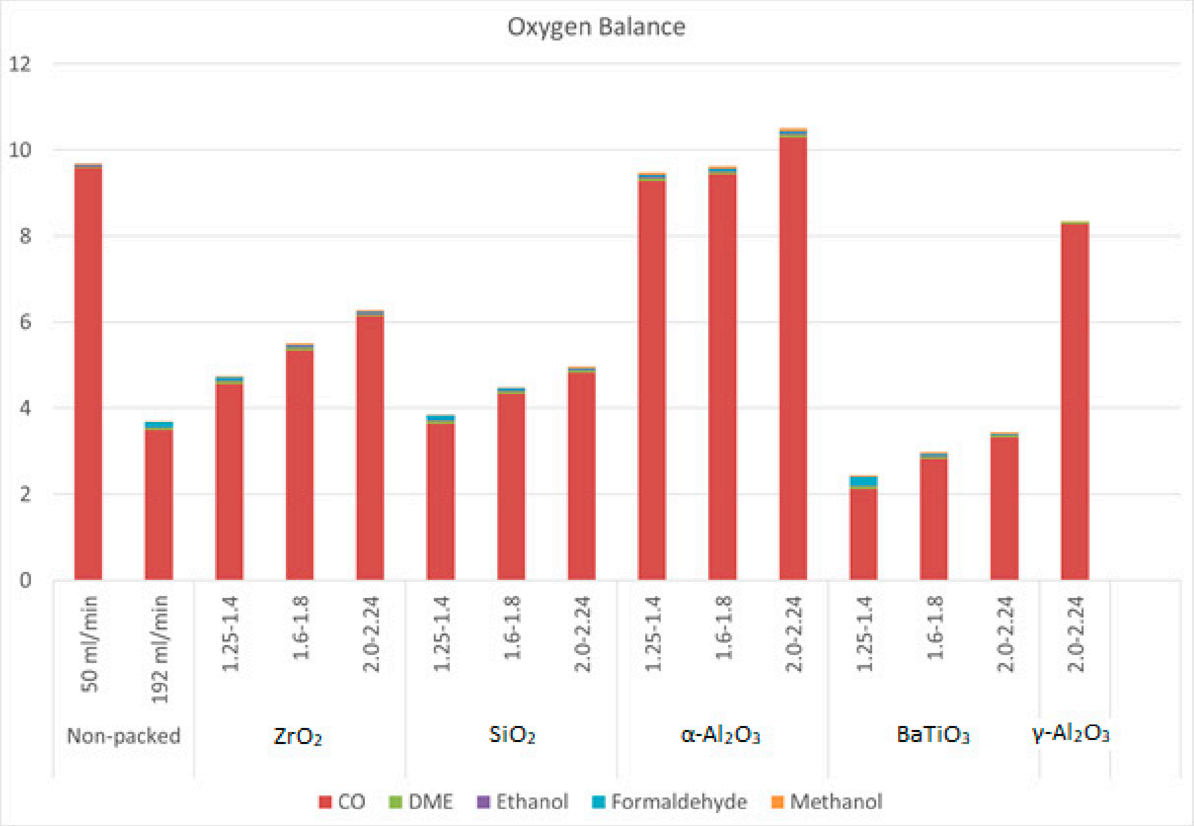

Figure S.32: Detailed oxygen balance for different sphere sizes and materials, without CO_2 contribution

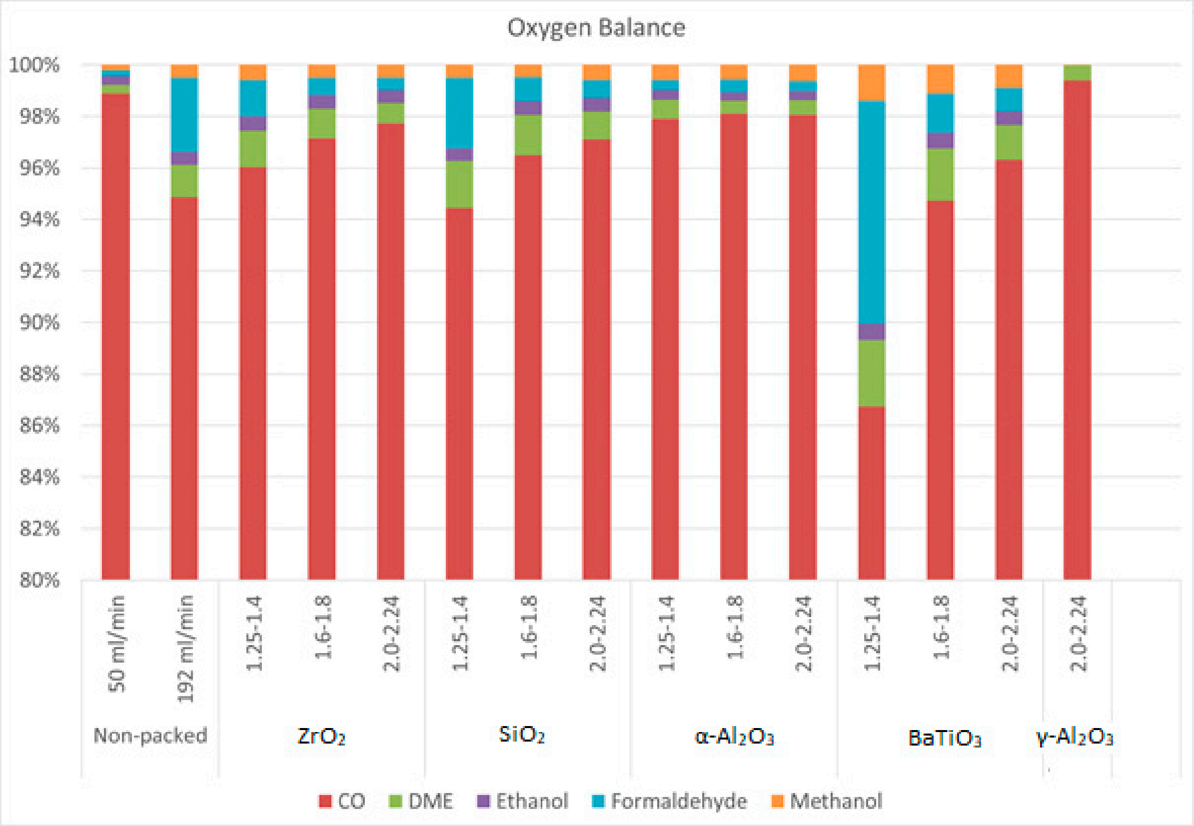

Figure S.33: Normalized oxygen balance for different sphere sizes and materials, without CO_2 contribution

6. YIELDS AND SELECTIVITIES

Table S.5: Identified products, ranked in decreasing order of their yields, for the different packing materials and the non-packed reactor. The components highlighted are present for more than 1%, the others for more than 100 ppm.

Non-packed	CO	C_2H_6	H_2	C_2H_2	C_3H_8	C_2H_4	CH_2O	C_2H_6O (DME)	C_2H_5OH (Ethanol)	CH_3OH
ZrO_2	CO	C_2H_6	C_2H_2	H_2	C_3H_8	C_2H_4	C_2H_6O (DME)	CH_2O	C_2H_5OH (Ethanol)	CH_3OH
SiO_2	CO	C_2H_2	C_2H_6	H_2	C_3H_8	C_2H_4	C_2H_6O (DME)	CH_2O	CH_3OH	C_2H_5OH (Ethanol)
α-Al_2O_3	CO	C_2H_6	H_2	C_3H_8	C_2H_2	C_2H_4	C_2H_6O (DME)	CH_3OH	CH_2O	C_2H_5OH (Ethanol)
γ-Al_2O_3	CO	C_2H_6	H_2	C_3H_8	C_2H_2	C_2H_4	C_2H_6O (DME)	CH_3OH	C_2H_5OH (Ethanol)	CH_2O
$BaTiO_3$	CO	C_2H_6	C_2H_2	H_2	C_3H_8	C_2H_4	C_2H_6O (DME)	CH_2O	CH_3OH	C_2H_5OH (Ethanol)

In the paper, we present the product fractions, since the yields and selectivities both have some terms that are subject to the gas expansion, which cannot be accounted for, due to the uncertainty on this gas expansion. However, for the sake of completeness, we also present here both qualitative information on the order of the product yields (Table S.5), and quantitative data on the selectivities (

Table S.6).

The yields and selectivities are calculated with the following formulas, illustrated for H_2.

$$Yield = [H_2]_{out} \tag{1}$$

$$Selectivity\ (\%) = \frac{2*[H_2]_{out}*100}{4*([CH_4]_{in}-[CH_4]_{out})} \tag{2}$$

Table S.6: Product selectivities (%) for the different packing materials and sizes, and for the non-packed reactor. The highest selectivities for each component are highlighted.

		CO	H_2	C_2H_6	C_2H_4	C_2H_2	C_3H_8	C_2H_6O (DME)	C_2H_5OH (Ethanol)	CH_2O	CH_3OH
Non-packed reactor	50 ml/min	31	4	15	3	4	6.2	0.2	0.2	0.1	0.1
	192 ml/min	26	4	23	3	6	5.9	0.7	0.3	0.8	0.1
ZrO_2	1.25-1.4	30	6	12	2	12	4.4	0.9	0.3	0.4	0.2
	1.6-1.8	29	5	12	1	10	4.4	0.7	0.3	0.2	0.1
	2.0-2.24	29	4	11	1	8	4.5	0.5	0.3	0.1	0.1
SiO_2	1.25-1.4	22	5	11	2	18	3.9	0.9	0.2	0.6	0.1
	1.6-1.8	21	4	9	2	14	4.0	0.7	0.2	0.2	0.1
	2.0-2.24	22	4	10	1	10	4.5	0.5	0.2	0.2	0.1
α-Al_2O_3	1.25-1.4	41	4	16	1	3	5.0	0.6	0.3	0.2	0.2
	1.6-1.8	38	4	15	1	3	4.4	0.4	0.3	0.2	0.2
	2.0-2.24	39	4	14	1	2	4.6	0.4	0.3	0.2	0.2
$BaTiO_3$	1.25-1.4	26	4	11	2	14	3.6	1.6	0.4	0.6	0.4
	1.6-1.8	32	5	13	2	12	4.0	1.3	0.4	0.5	0.4
	2.0-2.24	34	5	15	2	10	4.5	0.9	0.4	0.3	0.3
γ-Al_2O_3	2.0-2.24	36	4	16	1	2	4.6	0.4	0.0	0.0	0.0

7. REACTION SCHEMES FROM LITERATURE (DISCUSSION)

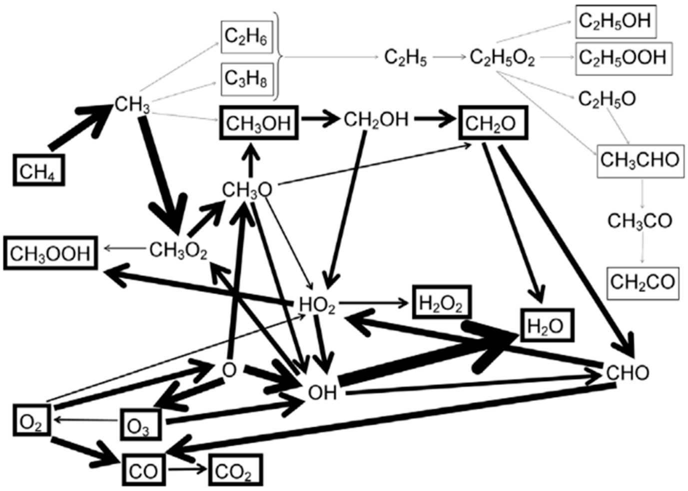

Figure S.34: Reaction scheme to illustrate the main pathways for the conversions of CH_4 and O_2 and their interactions. Adopted with permission from ref. [17]. **Copyright 2018 American Chemical Society**

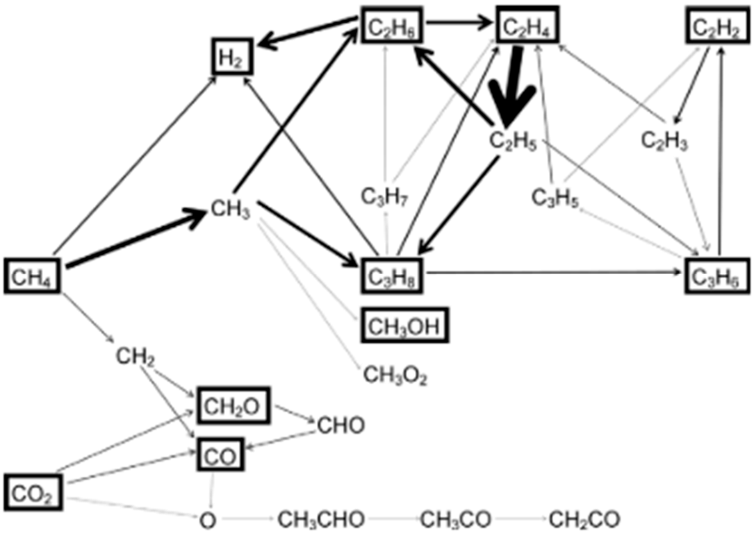

Figure S.35: Reaction scheme to illustrate the main pathways for dry reforming of methane. Adopted with permission from ref. [17]. **Copyright 2018 American Chemical Society**

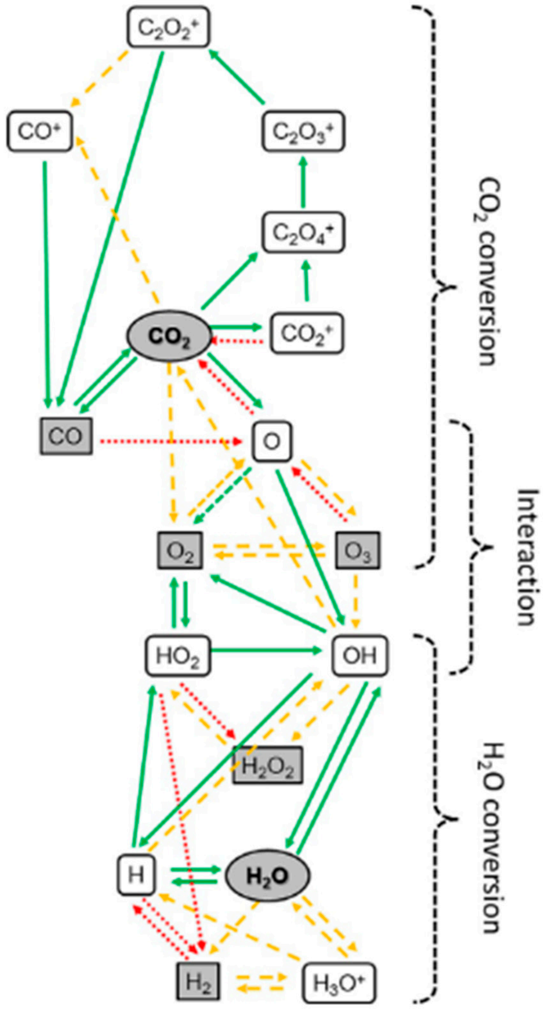

Figure S.36: Reaction scheme to illustrate the main pathways for the conversions of CO_2 and H_2O and their interactions. Adopted with permission from ref. [18]. **Copyright 2018 Wiley-VCH**

8. REFERENCES

1. Tojo, T.; Atake, T.; Mori, T.; Yamamura, H. Heat capacity and thermodynamic functions of zirconia and yttria-stabilized zirconia. *J. Chem. Thermodyn.* **1999**, *31*, 831–845.
2. Takahashi, Y.; Yokokawa, H.; Kadokura, H.; Sekine, Y.; Mukaibo, T. Laser-flash calorimetry I. Calibration and test on alumina heat capacity. *J. Chem. Thermodyn.* **1979**, *11*, 379–394.
3. Chase, M.W.J. *NIST-JANAF Themochemical Tables, J. Phys. Chem. Ref. Data*; 4th editio.; 1998;
4. He, Y. Heat capacity, thermal conductivity, and thermal expansion of barium titanate-based ceramics. *Thermochim. Acta* **2004**, *419*, 135–141.
5. Martienssen, W.; Warlimont, H. *Condensed matter and materials data*; 2005; ISBN 3-540-44376-2.
6. Zirconia - ZrO2, Zirconium Dioxide Available online: https://www.azom.com/properties.aspx?ArticleID=133.
7. Alumina - Aluminium Oxide - Al2O3 - A Refractory Ceramic Oxide Available online: https://www.azom.com/article.aspx?ArticleID=52.
8. Silica - Silicon Dioxide (SiO2) Available online: https://www.azom.com/properties.aspx?ArticleID=1114.
9. Butterworth, T.D. The Effects of Particle Size on CO2 reduction in Packed Bed Dielectric Barrier Discharge Plasma Reactors, 2015.

10. Lide, D.R. CRC Handbook of Chemistry and Physics. *J. Am. Chem. Soc.* **2009**, *131*, 12862–12862.
11. Michielsen, I.; Uytdenhouwen, Y.; Pype, J.; Michielsen, B.; Mertens, J.; Reniers, F.; Meynen, V.; Bogaerts, A. CO 2 dissociation in a packed bed DBD reactor: First steps towards a better understanding of plasma catalysis. *Chem. Eng. J.* **2017**, *326*, 477–488.
12. Piskunov, S.; Heifets, E.; Eglitis, R..; Borstel, G. Bulk properties and electronic structure of SrTiO3, BaTiO3, PbTiO3 perovskites: an ab initio HF/DFT study. *Comput. Mater. Sci.* **2004**, *29*, 165–178.
13. Chibisov, A.N. Effect of stoichiometry on the atomic and electronic structure of BaTiO3nanoparticles: A first-principles study. *Mol. Phys.* **2015**, *113*, 3291–3295.
14. Ramakanth, S.; James Raju, K.C. Band gap narrowing in BaTiO 3 nanoparticles facilitated by multiple mechanisms. *J. Appl. Phys.* **2014**, *115*, 173507.
15. Ahmed, R.; Sinnathambi, C.M.; Subbarao, D. Kinetics of de-coking of spent reforming catalyst. *J. Appl. Sci.* **2011**, *11*, 1225–1230.
16. Neyts, E.C.; Bogaerts, A. Understanding plasma catalysis through modelling and simulation—a review. *J. Phys. D. Appl. Phys.* **2014**, *47*, 224010.
17. De Bie, C.; Van Dijk, J.; Bogaerts, A. The Dominant Pathways for the Conversion of Methane into Oxygenates and Syngas in an Atmospheric Pressure Dielectric Barrier Discharge. *J. Phys. Chem. C* **2015**, *119*, 22331–22350.
18. Snoeckx, R.; Ozkan, A.; Reniers, F.; Bogaerts, A. The Quest for Value-Added Products from Carbon Dioxide and Water in a Dielectric Barrier Discharge: A Chemical Kinetics Study. *ChemSusChem* **2017**, *10*, 409–424.